Charles University
Faculty of Mathematics and Physics

DOCTORAL THESIS

2024 Vandana

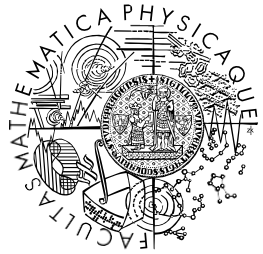

FACULTY
OF MATHEMATICS
AND PHYSICS

Charles University

DOCTORAL THESIS

Vandana

Development of dual-(+1)-Fluorescence Correlation Spectroscopy for Monitoring Protein Oligomerization Leading to Membrane Pore Formation

Ústav fyzikální chemie J. Heyrovského AV ČR, v. v. i.

Supervisor of the doctoral thesis: doc. RNDr. Radek Šachl, Ph.D.

Consultant: prof. Martin Hof, Ph.D., DSc.

Mathematics and Physics Faculty

Biophysics, Chemical and Macromolecular Physics

Prague 2024

I declare that I carried out this doctoral thesis independently, and only with the cited sources, literature and other professional sources. It has not been used to obtain another or the same degree.
I understand that my work relates to the rights and obligations under the Act No. 121/2000 Sb., the Copyright Act, as amended, in particular the fact that the Charles University has the right to conclude a license agreement on the use of this work as a school work pursuant to Section 60 subsection 1 of the Copyright Act.

In . . . . . date . . . .

Author's signature

Prohlašuji, že jsem tuto disertační práci vypracovala samostatně a pouze s použitím citovaných pramenů, literatury a dalších odborných zdrojů. Nebyla použita k získání jiného nebo stejného titulu.
Jsem srozuměn/a s tím, že se na mou práci vztahují práva a povinnosti podle zákona č. 121/2000 Sb. autorský zákon, ve znění pozdějších předpisů, zejména s tím, že Univerzita Karlova má právo uzavřít licenční smlouvu o užití tohoto díla jako školního díla podle § 60 odst. 1 autorského zákona.

V …… datum …… ……

Podpis autora

Dedication

I am deeply indebted to my supervisor, Radek Šachl, for his unwavering support, insightful guidance, and endless patience throughout my research journey. Thank you for providing me the opportunity to work in such a warm and intellectually stimulating environment, surrounded by bright and curious minds. I will always take pride in being your student and a member of your group. Your encouragement allowed me the freedom to explore and grow, while your readiness to offer guidance and support was a constant reassurance. Words cannot fully express my gratitude for all these years.

My heartfelt thanks also go to Sabina Macharová, who has been with me from the very beginning of my PhD journey to its conclusion. Her mentorship was essential to the completion of this thesis. Sabina trained me to work confidently in the lab, generously shared her vast knowledge of membranes, and guided me with the care and wisdom of a second mentor. I am equally grateful to Petra Riegerová, who played a pivotal role in my PhD journey. She was a constant source of motivation, lifting my spirits when challenges seemed insurmountable and offering invaluable assistance with protein-related problems.

A special note of thanks to Peter Kapusta, whose willingness to help with microscopic troubleshooting and teach the intricacies of microscopy was invaluable. Working alongside David Štástný on the same project was a pleasure; his reliability as both a friend and colleague was a true asset. I also owe a debt of gratitude to Barbora Svobodová for her consistent help in navigating the complexities of university bureaucracy.

I wish to express my sincere appreciation to Univerzita Karlova and the Czech Academy of Sciences for providing the resources and support that made this research possible. My thanks also extend to Mrs. Zádrapová, who was always just an email away, ready to assist students with their needs. I am also thankful to our collaborators from Heidelberg, Prof. Nickel Walter and his group for their work on FGF2 protein purification and for the fruitful discussions that have enriched this research.

I also deeply appreciate my previous supervisors from my master's and bachelor's studies, Prof. H.B. Bohidar, Asst. Prof. Kamla Rawat, and Asst. Prof. Aditi Gupta, whose encouragement and guidance laid the foundation for this journey.

My deepest gratitude goes to the Room 215 gang members, whose love, patience, and unwavering belief in me have been my anchor throughout this journey. I would like to extend my thanks to my dear friends who stood by me through the ups and downs of failed experiments: Darina, Barbora, Petra, Isabel, David, Garima, Abhinav, Hyusein, Federica, David, Arunima, Harsha, Honza, Katka, Alfredo, Zuzana, and Tej.

I also want to mention Martin, Petra, Pawel, Matej, Piotr, Agnieszka, Sarka, Tomas, Marek, Mariana, and Honza; thank you for your care, guidance and for setting a high standard to aspire to. I am grateful to my colleagues and friends from the HOF fluorescence group, whose camaraderie, motivation, and insightful discussions have enriched my research and made the journey even more rewarding.

To my friends in Prague—Poonam, Tania, Katarina, Nadiya, Silvia, Laxmi, Banhi, Sarra, Alex and the Mazankaian group—your friendship has been a source of immense support. I would also like to thank the Majovská family for organizing wonderful weekend gatherings and secret cafes gatherings, as well as Teresa for organizing memorable experiences like Ochutnávka vín.

To my friends back in India—Shalki, Abhishek, Navkiran, Devender, Sudipto, Satya, Abinash, Avdhesh, Rahul, Pravi, Surojit, Srishti, Priyanka and Pankaj—thank you for your unwavering encouragement, even from afar.

I want to extend my thanks to ChatGPT and the advancements of the AI era, which have provided me with valuable assistance, insights, and support during my research. The ability to engage with AI tools has made the complexities of this journey a bit easier to navigate, and I am grateful for this technological support. To all who have played a part in this journey, I offer my heartfelt thanks. This thesis would not have been possible without your support.

To all who have played a part in this journey, I offer my heartfelt thanks. This thesis would not have been possible without your support. Especially to my family, who instilled in me the values of education and hard work and whose love and encouragement have been my constant source of strength.

Title: Development of dual-(+1)-Fluorescence Correlation Spectroscopy for Monitoring Protein Oligomerization Leading to Membrane Pore Formation.

Author: Vandana

Department: Biophysics, chemical and macromolecular physics

Supervisor: doc. RNDr. Radek Šachl, Ph.D.,

Abstract: This dissertation introduces on the example of fibroblast growth factor 2 (FGF2) protein, a new statistical approach that can differentiate 'functional' membrane-inserted oligomers from 'non-functional' protein aggregates associated with membranes. Its application extends not only to FGF2 but also to many other membranes associated proteins that induce the formation of membrane pores. The principle of this approach is based on dual-color fluorescence correlation spectroscopy (FCS) applied to single giant unilamellar vesicles (GUVs). By analyzing the brightness and diffusion properties of fluorescently labeled proteins, it provides crucial insights into the protein oligomeric size, diffusion coefficients, surface concentrations, and membrane permeability on free-standing membrane parts of GUVs. It operates at a broad range of protein surface concentrations, allowing for a deeper exploration of protein oligomerization. Specifically tailored for studying membrane proteins, the dual-(+1)-FCS method stands out for its ability to comprehensively analyze multiple parameters in a single experiment. Overall, our methodology provides a robust tool for correlating membrane protein oligomerization with membrane pore formation and opens new avenues for understanding multimodal distributions of oligomeric states commonly obtained by single-molecule microscopic methods.

Keywords: dual-(+1)-FCS, FGF2, Oligomerization, membrane, pore formation.

Title: Vývoj duální-(+1)-fluorescenční korelační spektroskopie pro sledování oligomerizace proteinů vedoucí k tvorbě membránových pórů

Author: Vandana

Department: Biofyzika, chemická a makromolekulární fyzika

Supervisor: doc. RNDr. Radek Šachl, Ph.D.,

Abstrakt: Tato disertační práce představuje na příkladu fibroblastového růstového faktoru 2 (FGF2) nový statistický přístup, který dokáže odlišit „funkční“ oligomery vložené do membrán od „nefunkčních“ proteinových agregátů spojených s membránami. Jeho použití se rozšiřuje nejen na FGF2, ale i na mnoho dalších proteinů asociovaných s membránami, které vyvolávají tvorbu membránových pórů. Princip tohoto přístupu je založen na dvoubarevné fluorescenční korelační spektroskopii (FCS) aplikované na jednotlivé obří unilamelární vezikuly (GUV). Analýzou jasu a difúzních vlastností fluorescenčně značených proteinů poskytuje zásadní poznatky o velikosti oligomerů proteinů, difúzních koeficientech, povrchových koncentracích a propustnosti membrán na volně stojících částech membrán GUVs. Pracuje v širokém rozsahu povrchových koncentrací proteinů, což umožňuje hlubší zkoumání oligomerizace proteinů. Metoda dual-(+1)-FCS, speciálně přizpůsobená pro studium membránových proteinů, vyniká schopností komplexně analyzovat více parametrů v jediném experimentu. Celkově naše metodika představuje robustní nástroj pro korelaci oligomerizace membránových proteinů s tvorbou membránových pórů a otevírá nové možnosti pro porozumnění multimodálním distribucím oligomerních stavů běžně získávaným pomocí mikroskopických metod s citlivostí na jednotlivé molekuly.

Klíčová slova: dual-(+1)-FCS, FGF2, oligomerizace, membrána, tvorba pórů

Table of Contents

Introduction

The membrane is an intriguing and complex system to study, playing a critical role in regulating the biochemical processes that occur within and outside of cells. It serves as a dynamic barrier that protects cellular components and facilitates communication and transport from the intracellular to the extracellular environment or the other way around [1–5]. Examining the membrane at the nanoscale level reveals the presence and behaviour of proteins embedded within or associated with the membrane, providing valuable insights into their intricate interactions and functions. Proteins within the membrane exhibit a variety of behaviours and functions that are essential for cellular life. For example, some membrane proteins aggregate to form pores or channels, which are vital for import-export molecules such as nutrients, ions and many more through the membrane [6, 7]. These aggregates can be highly specific and regulated, responding to cellular signals and environmental conditions to maintain homeostasis. The study of such protein aggregations is essential for understanding how cells control permeability, signalling, and energy transduction.

A membrane pore can be characterized as a localized disturbance in the membrane that facilitates the passive movement of molecules [8]. Pore-forming proteins (PFPs) are a large and diverse protein family that all share the function of pore generation to alter membrane permeability [9–13]. These proteins can function externally by being secreted as soluble proteins, inducing permeabilization in the plasma membrane of their designated target cells. Notably, this encompasses various pore-forming toxins (PFTs), potent virulence factors in nature, and perforin is secreted by Natural Killer cells (NK) and cytotoxic T cells [11, 14–16]. PFPs play an essential role in various biological processes [17, 18]. Various organisms use pore-forming proteins for diverse purposes, such as defence strategies in pathogenic bacteria and eukaryotic organisms [19, 20]. In higher vertebrates, PFPs play pivotal roles in defence mechanisms against pathogens, serving as critical executioners in the generation of inflammatory responses [21, 22].

PFPs can function as intracellular killers in the context of cell death signalling pathways [23, 24]. For example, the BCL-2 family's proteins make pores and permeabilize mitochondrial membrane (MOM) in process of the intrinsic apoptosis process. Gasdermin (GSDMs) carry out pyroptosis by a process that results in the opening of pores in the plasma membrane (PM). The process by which the mixed lineage kinase domain-like (MLKL) drives permeabilization

of the plasma membrane during necroptosis is not entirely understood. However, it may be linked to pore creation [25–27]. Pore-forming proteins (PFPs) are generally classified as α or β based on the secondary structure of the protein segments that form the pore. These proteins can create various types of pores, which are distinguished by whether lipids are involved in their structure. Pores can be categorized as protein-lined, pure lipid, or protein-lipid, depending on their composition. In protein-lined pores, the lumen is formed entirely by transmembrane segments of the proteins, which can arrange into either α-barrel or β-barrel structures. [9, 14].

The membrane or specific membrane lipids often play a critical role in the recruitment, assembly, and folding of proteins in these types of pores [9, 28]. In the context of regulated cell death, various endogenous pro-death effectors employ a range of strategies to permeabilize cellular membranes. The structure of the resulting pores is determined by the specific combination of proteins and lipids, along with their intramolecular interactions. This composition influences the heterogeneity, size, and stability of the pores, which in turn affects the types of molecules that can pass through. Consequently, the properties of these membrane pores have a significant impact on the signaling pathways activated following membrane permeabilization.

Pore formation is a crucial step in the signaling pathways that drive various forms of regulated cell death. Proteins like BAX/BAK, gasdermins (GSDMs), and mixed lineage kinase domain-like protein (MLKL) are key players in creating membrane pores with distinct properties, which govern the movement of molecules across membranes and ultimately determine the cell's fate. These proteins also play an essential role in controlling the type and timing of the release of cellular contents and their impact on the organism. Understanding the regulation and assembly of membrane pores offers significant potential for developing new strategies to control cell death and modulate the inflammatory and immunological effects of these processes for therapeutic purposes [18].

Given the interdependence of many cell death pathways, several PFPs can be active at the same time in a population of challenged cells. Different cytokines, chemokines, and damage-associated molecular patterns may be released as a result of the coexistence of cell death modes, which may have significant physiological and pathological ramifications. Gaining knowledge of PFPs' functions and interactions in membrane biology can help create new treatment modalities for a range of illnesses.

The Mechanism of Pore Formation

The overall process of pore formation usually involves a series of four steps. These include directing the activated protein to the membrane, inserting it into the membrane, undergoing oligomerization, and finally, assembling the pore (refer to **Figure 1A**). Although these steps are shared among all PFPs, the specific sequence of events can vary among different classes of PFPs, as outlined in **Figure 1** [28–31].

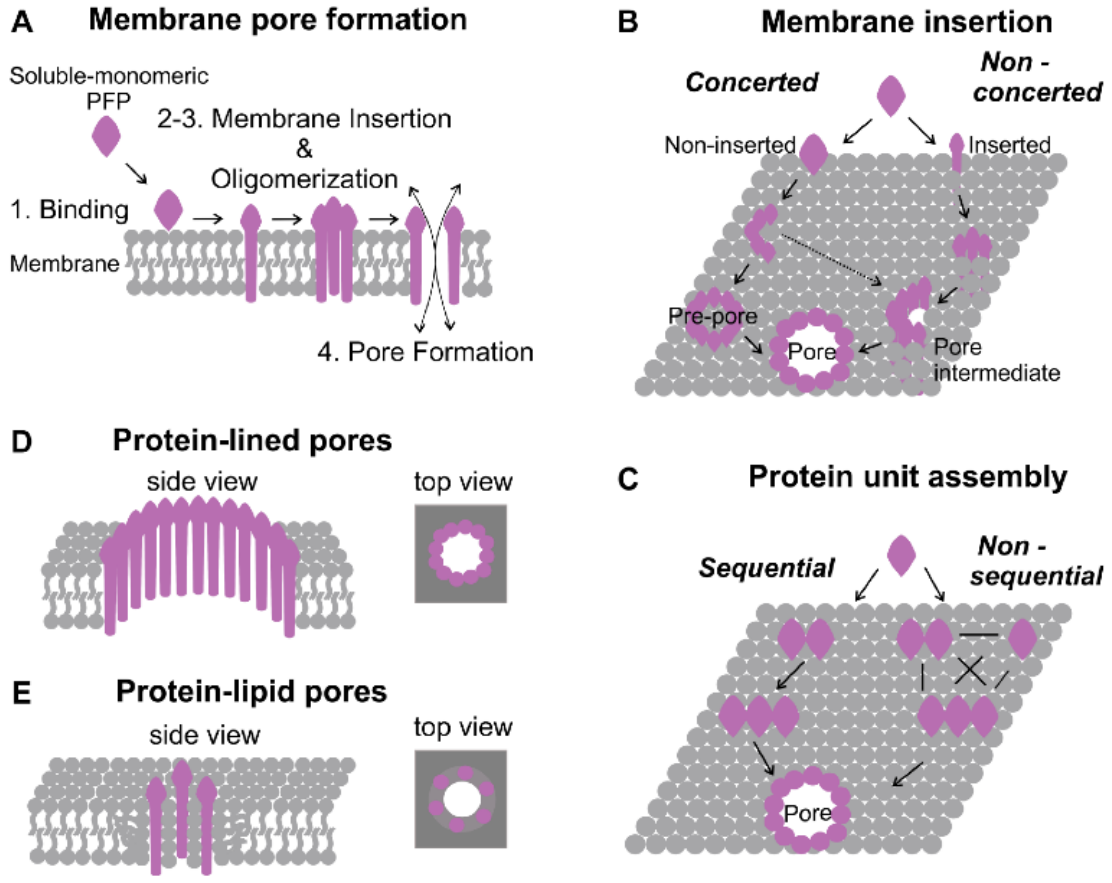

Figure 1: Illustrative Overview of Pore Formation in Membranes by PFPs: (A) This diagram details the stages of membrane pore formation by pore forming proteins (PFPs), including binding, membrane insertion, oligomerization, and pore formation. (B) It also explores the dynamics of membrane insertion and protein unit assembly, both concerted and non-concerted ways of insertion. (C) Protein assembly mechanism: sequential versus non-sequential. Protein oligomerisation can happen when units of a defined stoichiometry are added one after the other sequentially or randomly (non-sequentially). (D&E) visual representations of protein-lined and protein-lipid pores in side and top views: protein-lined pores (pores formed by proteins only) & Protein-lipid pores (pores formed by both lipids and proteins). (The figure was adapted from "https://doi.org/10.3390/ijms24054528").

Artificial membrane systems

Cellular membranes are crucial for protecting cells from their external environment and helping in various cellular functions, such as substance exchange, cell adhesion, transport, metabolism, and signaling. These membranes consist of complex networks of proteins embedded within a lipid bilayer, which includes a wide variety of lipid species. The complexity and diversity of these components make it difficult to isolate and understand the specific roles of proteins and lipids in cellular functions.

Model membranes address this challenge by providing simplified membrane systems where individual components can be introduced and studied in a controlled manner. This approach facilitates the identification of the distinct roles that proteins and lipids play in the functional activity of pore-forming proteins [32–34]. By utilizing model membranes system, it offers a significant advantage in unraveling the intricate mechanisms of biological membranes.

On one hand, these model systems allow researchers to explore how individual lipids—considering factors such as lipid charge, geometry, and the length and saturation of fatty acyl chains—contribute to protein function and impact membrane properties like curvature and fluidity. On the other hand, reconstituting purified proteins into lipids enables a more focused investigation of specific interactions and functions.

Model membranes, often in the form of free-standing lipid vesicles, are widely used for such studies (see Figure 2). These vesicles, which are spherical assemblies of lipid bilayers encasing an aqueous compartment, vary in size: small unilamellar vesicles (SUVs) are less than 50 nm in diameter, large unilamellar vesicles (LUVs) range from 100 nm to 1 μm, and giant unilamellar vesicles (GUVs) are larger than 1 μm. SUVs and LUVs are typically generated by disrupting multilamellar liposomes through various physical methods, such as extrusion, sonication/ultrasonication, or detergent dialysis and homogenization [33, 35]. On the other hand, GUVs can be formed by electroformation and gel-assisted method [36, 37].

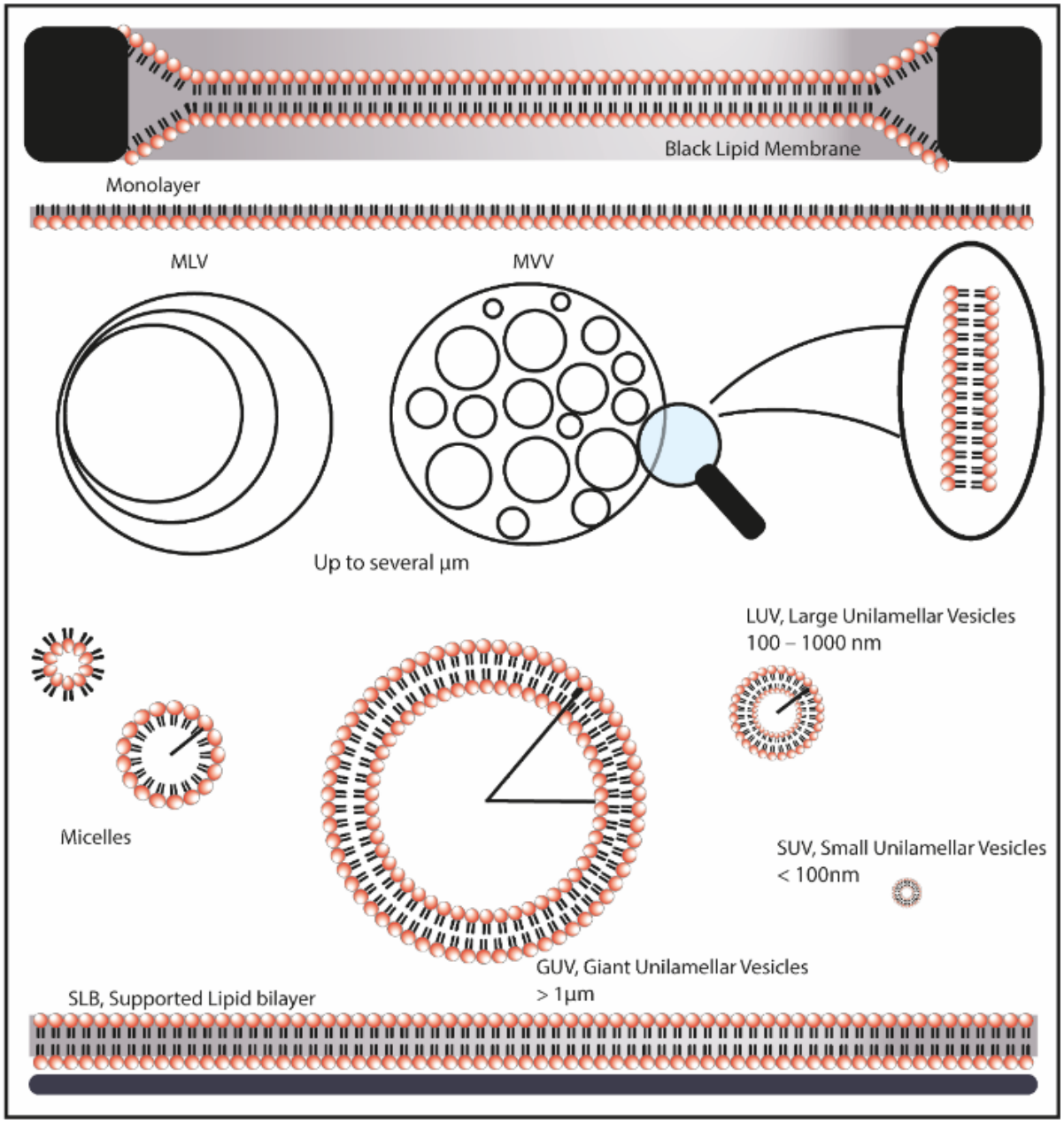

Figure 2: Free-standing model membrane systems represented by black lipid membranes, SUVs, LUVs or GUVs and supported lipid bilayers systems.

Supported phospholipid bilayers (SPBs) are a widely used membrane model system known for their flat structure, which is formed on planar surfaces with a thin liquid layer separating the bilayer from the underlying surface (**Figure 2**) [38]. SPBs are typically created on hydrophilic, smooth substrates such as glass, mica, or silica. These materials facilitate the spontaneous formation of bilayers through the adsorption of vesicles, followed by their fusion, a process that is often enhanced by the presence of calcium ions [39–41].

One of the key advantages of SPBs, compared to free-standing vesicles, is their planar configuration. This flat structure eliminates the effects of membrane curvature, making SPBs particularly suitable for various biophysical techniques. However, a significant challenge arises when incorporating transmembrane proteins into SPBs. The thin hydration layer between the support and the bilayer may be insufficient, leading to unwanted interactions between the proteins and the supporting surface. Such interactions can result in the fixation of proteins, potentially causing protein deformation or denaturation.

To overcome this limitation, a polymeric layer can be introduced as a spacer between the substrate and the lipid bilayer, resulting in polymer-supported membranes (PSMs). PSMs address this issue by allowing proteins to diffuse within the bilayer and enabling real-time tracking of protein assembly [42–44]. PSMs have been used, for example, to study the redistribution of cholera toxin subunit B toward liquid-ordered domains within the membrane [45]. Additionally, PSMs have been applied in detecting membrane pore formation induced by α-hemolysin in membrane biosensors, where a membrane bilayer is formed on a conducting polymer [46].

Nanodiscs are disc-shaped, soluble phospholipid bilayers encased by a protein belt, capable of incorporating integral membrane proteins. They offer a versatile platform for functional and structural studies, characterized by their uniform size and remarkable stability in aqueous environments, which provides access to both sides of the lipid bilayer [47, 48]. These features make nanodiscs essential tools for protein structural analysis using techniques like AFM, NMR, and cryo-EM microscopy.

In summary, model membrane systems serve as essential instruments for analyzing the mechanisms and structures of PFPs. Nevertheless, it's crucial to acknowledge that these systems offer a simplified representation of cellular processes. Consequently, they should be viewed as a supplementary rather than a replacement approach for assessing protein complexes within their natural physiological cellular context.

1. Techniques for studying membrane pore formation & protein oligomeric states

Over the past decades, various biophysical techniques have been extensively used to study the functional properties of membrane pores [49, 50] While atomic force microscopy (AFM), electron microscopy (EM), and X-ray crystallography are commonly used for obtaining structural information, they often fall short in capturing the intricate dynamics of membrane pore formation. Complementary approaches have thus been developed, involving stepwise photobleaching, (single-molecule) Förster Resonance Energy Transfer (smFRET), Fluorescence Cross-Correlation Spectroscopy (FCCS), or super-resolution microscopy[51–56]. To gain a deeper insight into the molecular mechanisms of pore-forming proteins, it is crucial to characterize pore structures at a single-entity level. In this context, in the next chapter, we explore different methods commonly utilized for the functional and structural characterization of membrane pores, involving membrane permeabilization approaches and methods enabling the monitoring of protein self-assembly (oligomerization) into membrane pores.

Membrane permeability

Membrane permeabilization (pore formation) monitored by fluorescence leakage assays:

A prevalent method for investigating membrane permeabilization involves monitoring the passage of fluorescent markers through the lipid bilayer. Various techniques have been developed for this purpose over time. In terms of quantifying the amount of permeabilized (leaky) vesicles, two approaches became widely popular: (1) a bulk method utilizing LUVs loaded with calcein dye and (2) a single vesicle assay employing GUVs. Both methods provide information about the fraction of leaked vesicles and the kinetics of released dye, offering comprehensive insights into the mechanism of membrane permeabilization.

1.1 leakage assay on LUVs & GUVs

Certain fluorescent dyes, including calcein, possess the ability to be self-quenched at elevated bulk concentrations, with calcein exhibiting self-quenching above 1mM [57]. In this

approach, LUVs are prepared in a concentrated calcein solution (typically 30 – 100 mM) and subsequently undergo size exclusion chromatography to eliminate unencapsulated free dye (**Figure 3(a)**). Upon permeabilization of the LUV's membrane, entrapped calcein is released (**Figure 3(b)**). As it becomes diluted, the dye starts to fluoresce, allowing the monitoring of pore formation through time-co-operated fluorescence intensity measurements. To achieve maximum fluorescence intensity (F_∞) and release of all entrapped dye, detergent is introduced at the end of the measurement.

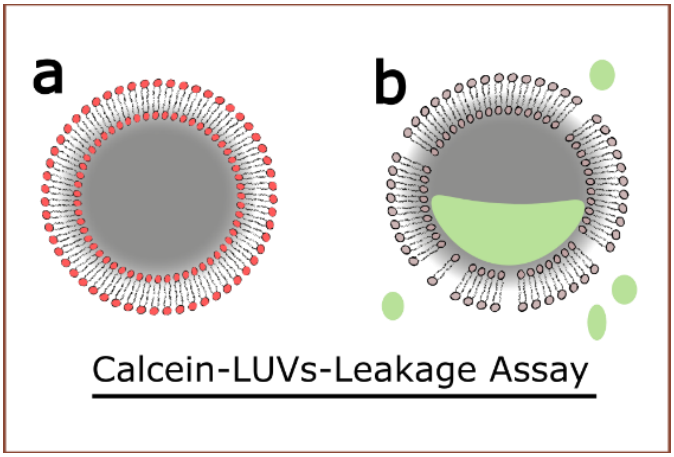

Figure 3: The principle of LUVs leakage assay based on the release of calcein from the LUV interior. The LUV in (a) represents a calcein loaded vesicle at self-quenching concentration, whereas the LUV in (b) represents a leaky LUV with partially released dye.

To monitor the fraction of permeabilized vesicles over time, normalized fluorescence intensity is usually calculated according to:

$$F_n = \frac{F_t - F_0}{F_\infty - F_0} \tag{1}$$

Where F_n is the normalized fluorescent intensity, F_t is the fluorescent intensity at time t, F_∞ is the maximal fluorescence intensity obtained after the detergent addition, and F_0 is the background intensity.

Assuming a continuous flux of matter through the vesicle membrane, J, the kinetics of calcein release can be fitted by the following equation [58]:

$$F_n = F_n^0 \left(1 - e^{\frac{-3 \cdot J(t - t_0)}{r}}\right) \tag{2}$$

The flux J across the lipid bilayer aligns with the concentration gradient, representing the rate at which molecules diffuse through the lipid bilayer. In equation 2, F_n^0 represents the degree of leakage (alternatively the fraction of leaky vesicles), r is the vesicle radius, t is the time, and t_0 is the initial time when leakage starts.

Leakage assay using GUVs

GUVs with diameters typically ranging from 10 to 100 μm are sufficiently big enough to be observed under a conventional microscope. A well known benefit of this approach, the continuous visualization of individual vesicles during the entire experiment, enabling the monitoring of membrane stability during leakage (**Figure 4**). Additionally, complementary processes like changes in vesicle structure, fusion with other vesicles, or budding on vesicles can be captured. To do the fluorescent imaging measurements, a suitable lipid soluble fluorescent dye is utilized to detect and monitor the vesicles. Water soluble (Hydrophilic) fluorescent dye is added to the media surrounding the GUVs to probe the leakage. An essential characteristic of leakage involves distinguishing between the mechanisms known as "all-or-none" or "graded." The former describes a condition when vesicles either leak entirely or not at all, indicating stable pores over time. The latter refers to a process in which vesicles release only a portion of their content [59, 60]. Using GUVs, the evaluation encompasses both the percentage of leaked vesicles and the fluorescent intensity within each GUV. As a result, the graded and all-or-none leakage mechanisms can be directly distinguished.

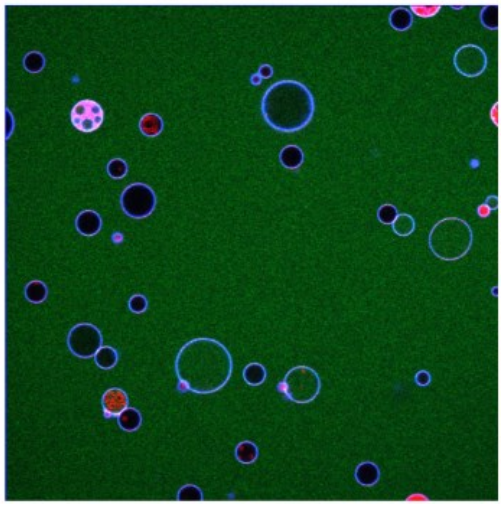

Figure 4: Confocal microscopy images of non-leaky GUVs (the GUV's interior is black) and leaky GUVs (the GUV's interior is green). 'Green' fluorescent dye Alexa-Fluor-532 has been added to the GUV exterior.

The extent of leakage for each GUV can be determined according to the following equation:

$$F_n = \frac{F_v - F_b}{F_{out} - F_b} \quad (3)$$

Here F_v represents the average intensity per pixel present in the GUV, F_{out} represents the initial fluorescence intensity per pixel surrounding the vesicle, and F_b is the average background intensity per pixel.

Measuring protein oligomeric states leading to membrane pore formation

1.2 Chemical Crosslinking

A traditional approach for assessing the size of protein oligomers involves chemically crosslinking the subunits within the complex. Developed in the late 1970s, this technique creates stable bonds—usually through amines or sulfides—between various protomers in an oligomer. To perform this, cells are exposed to chemical crosslinkers like formaldehyde or bis-(2-methanethiosulfonatoethyl) amine hydrochloride (bis-EA). During this process, only proteins in close proximity, such as those within an oligomer, form covalent bonds [61–63]. After crosslinking, proteins bound to the plasma membrane are extracted from the membrane.

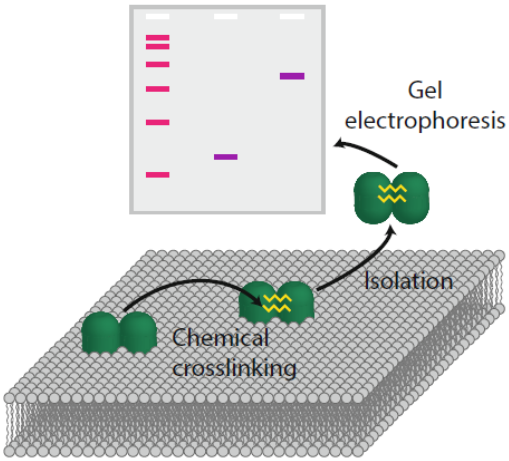

Figure 5: Chemical Crosslinking: an in-vitro approach to investigate protein oligomerization. (Figure was adapted from "https://doi.org/10.1007/978-3-319-66601-3_8").

The proteins of interest are then isolated from the mixture using techniques like immunoprecipitation or other affinity methods. Subsequently, the size of the isolated oligomers is determined using Sodium Dodecyl Sulfate-Polyacrylamide Gel Electrophoresis (also known as SDS-PAGE) in combination with Western blotting. This classical approach has been fundamental in studying protein interactions and determining the oligomeric size of proteins (see **Figure 5** for a basic setup of a cross-linking experiment).

Chemical crosslinking allows scientists to investigate protein-protein interactions in their native biological context. It can capture transient or weak interactions that may be lost during traditional protein purification. Unlike some techniques that require denaturation, crosslinking is performed under mild conditions, preserving the native conformations of proteins. When combined with other structural biology methods like mass spectrometry or electron microscopy, chemical crosslinking can provide structural information about protein complexes and their oligomeric states. It is applicable to a wide range of proteins and complexes, making it versatile for various biological systems.

In comparison to other approaches (see below), chemical crosslinking can be considered a rapid and 'cheap' approach for assessing the oligomerization states of proteins as it does not need any specialized equipment or chemical reagents, rendering it accessible and widely utilized in the scientific community. Its versatility extends to both hetero- and homo-oligomerization scenarios[64]. However, inherent limitations exist within this technique as the applied experimental conditions are still too harsh and away from the native cellular environment. Consequently, it may generate artificial clusters that lack stability in their native membrane environment. Additionally, when the reactive sites in the protein oligomer are too distantly spaced, crosslinking efficiency diminishes.

Moreover, the interpretation of oligomeric populations from gel electrophoresis lacks sensitivity, leading to potential oversight of minority populations. It also lacks real-time measurement capabilities and spatial resolution. Moreover, the choice of a crosslinker and conditions must be carefully optimized to ensure specific and meaningful crosslinking without introducing artefacts. Finally, data interpretation can be complex, especially for large protein complexes, as multiple crosslinking sites can be involved.

1.3 High-resolution localisation microscopy

Numerous or even countless fluorophores are present in a typical fluorescently labeled biological sample at a high density, making it challenging to distinguish them using the single-molecule localization method. A recent breakthrough addresses this challenge by differentiating the otherwise spatially overlapping fluorescent signals in the time domain, utilizing fluorescent probes that can switch between a fluorescent and a dark state.This method allows molecules to be individually imaged, localised, and then deactivated by activating them at different times within a diffraction-limited zone (**Figure 6**). Wide-field imaging enables massively parallel localization, allowing for the mapping of several fluorophores' coordinates and the subsequent reconstruction of super-resolution images. Three labs independently came up with and carried out this notion, which they named STORM, PALM, and FPALM, respectively. Initially, photo-switchable fluorescent dyes or proteins—which are triggered by light with a wavelength distinct from the imaging light that causes fluorescence to excite and fluorophores to deactivate—were utilised in all three labs. By keeping activation and imaging distinct, it is possible to regulate the proportion of fluorescent molecules at any given moment, enabling accurate localization and optical separation of the active molecules. Numerous fluorophores can then have their locations recorded and used to create a super-resolution image by repeating the activation and imaging procedure. We call this method "super-resolution microscopy by single-molecule localization" in the following. Subsequent reports have described additional variations of this strategy that use non-optical phenomena, including the stochastic binding of diffuse fluorophores or asynchronous fluorophore activation and deactivation. These super-resolution approaches have then been used in the research of membrane pores [65].

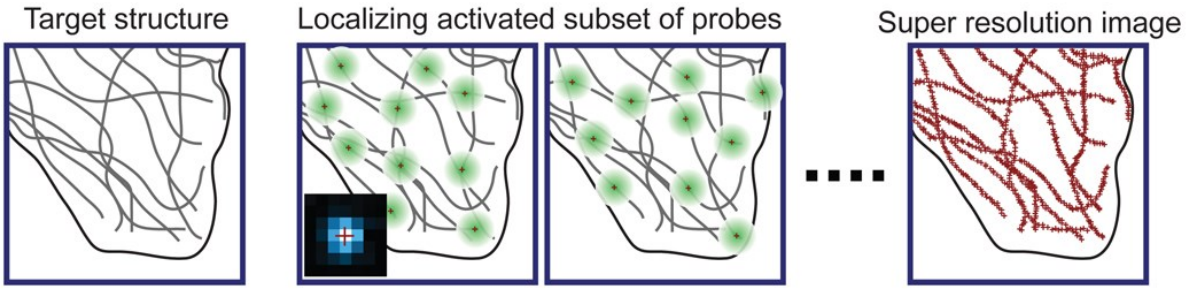

Figure 6: The idea behind PALM, FPALM, and STORM. The subsets of fluorophores can be observed without spatial overlap and precisely localised thanks to the distinct fluorescent probes indicating the sample structure that are activated at different times. Numerous fluorescent probes can have their positions identified by repeating the activation and

imaging process. A super-resolution image can then be rebuilt using the locations of multiple localised probe molecules. The lower left inset of the second panel displays an experimental image of a single fluorescent dye (blue) alongside the high-precision localization of the molecule (red cross). (The figure was adapted from "10.1146/annurev.biochem.77.061906.092014").

1.4 STED microscopy

The concept of stimulated emission depletion (STED) microscopy was proposed in 1994 and later demonstrated experimentally. It uses a second laser (STED laser) to suppress fluorescence emission from fluorophores outside the excitation center. This suppression occurs through stimulated emission, where an excited fluorophore returns to the ground state when encountering a matching photon, depleting excited fluorophores capable of emitting fluorescence [66, 67](**Figure 7(A, B)**). As a result, fluorescence is emitted from a small spot, its size being considerably below the diffraction limit of the light used.

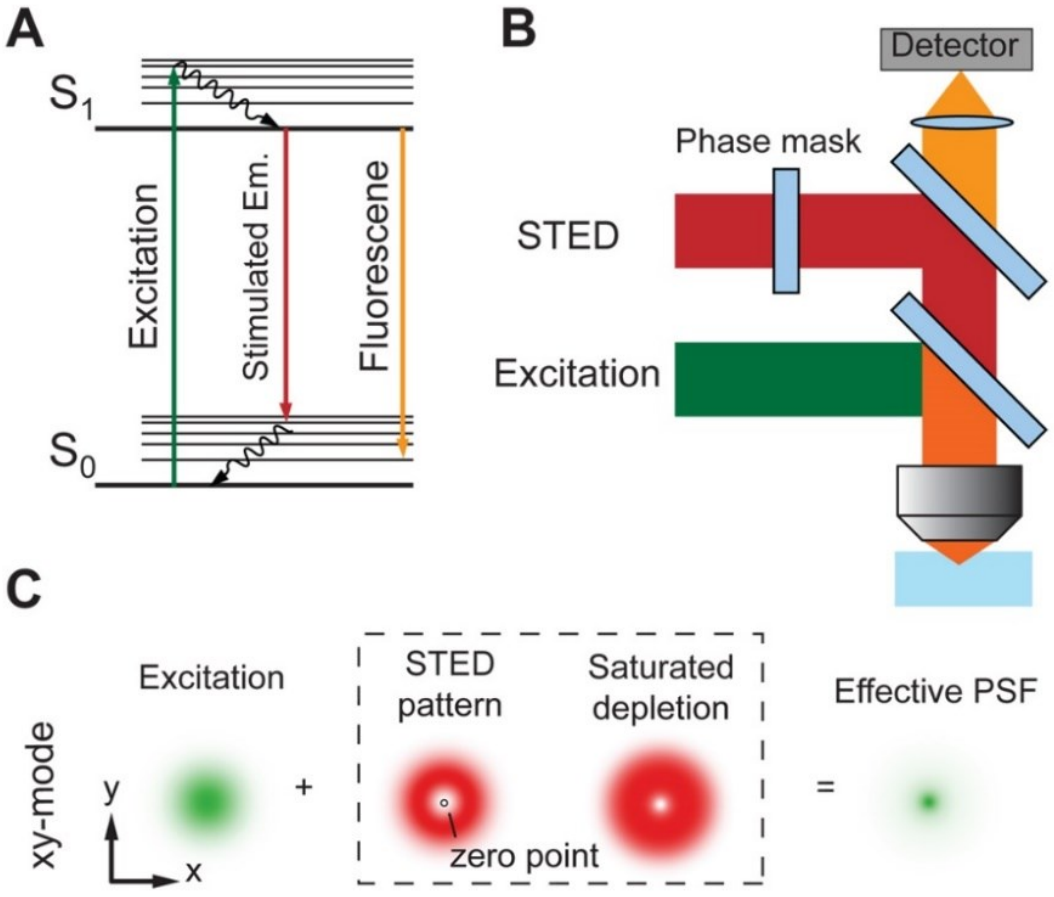

Figure 7: This image represents the principle of STED microscopy. (A) The mechanism of stimulated emission. (B) A diagram illustrating a STED microscope. (C) In XY mode, a doughnut-shaped STED laser is used, with its zero point aligned to the peak of the excitation laser focus. Through saturated depletion, fluorescence from areas near the zero point is suppressed, leading to a smaller effective PSF size. (The figure was adopted from "10.1146/annurev.biochem.77.061906.092014").

Achieving super-resolution relies on the nonlinear relationship between the depleted population and the intensity of the STED laser as it nears saturation. When the local intensity of the STED laser exceeds a specific threshold, nearly all spontaneous fluorescence emission is suppressed. Increasing the power of the STED laser expands the saturated depletion zone without significantly impacting fluorescence emission at the focal point, where the STED laser intensity is minimal. This restriction confines fluorescence signal detection to a narrow area around the focal point, thereby reducing the effective width of the point spread function (**Figure 7C**). The extent of this area is constrained by the operational power of the STED laser rather than by light diffraction.

Super-resolution images are subsequently generated by scanning this compact, effective PSF. While theoretically, the spatial resolution of STED microscopy can be pushed to unlimited scales, practical limitations related to the photophysical properties of fluorophores under physiological conditions limit the achievable lateral resolution to approximately 20–50 nm in cell studies. STED microscopy imaging, like confocal microscopy, involves sequential raster-scanning of the sample, which makes image acquisition too slow to track individual diffusing molecules. STED has been used on biological materials that have been genetically tagged with fluorescent proteins (FPs)), or immunostained with fluorophore-labeled antibodies [68]. Large stimulated emission cross sections in the visible to near-infrared (IR) region and robust photostability under STED conditions are desirable for the used dyes. Among the most widely used dyes for STED microscopy are Atto 532 and Atto 647N. As shown later in this work, STED has successfully been employed to determine oligomeric states of membrane-associated fibroblast growth factor 2 proteins that form membrane pores [69].

1.5 Number and Brightness Analysis

Number and Brightness (N&B) analysis is a computational method used in fluorescence microscopy to study the number, brightness, and oligomeric states of molecules within biological samples[70–75]. This technique is valuable for understanding molecular interactions and dynamics in cellular systems. Below is a brief explanation of N&B analysis:
N&B analysis leverages fluctuations in fluorescence signals originating from varying numbers of molecules within individual pixels of a microscope image. By analyzing both the mean and variance of fluorescence intensity distributions, researchers can evaluate two key parameters:

Average Number of Molecules: The ratio of the square of the average intensity to the variance of the fluorescence signal is proportional to the average number of particles contributing to the signal. A larger variance indicates fewer contributing molecules.

$$n = \frac{\langle k \rangle^2}{\sigma^2 - \langle k \rangle} \tag{4}$$

The term *n* symbolizes the average number of molecules in the illumination volume, $\langle k \rangle$ is the average counts, and σ is the variance.

Brightness: The brightness of individual molecules can be assessed based on their fluorescence intensity. The molecular brightness ε is defined as the amount of photons emitted per second per molecule when the molecule is located in the middle of the illumination volume. In biological contexts, this brightness serves as an indicator of the clustering or aggregation status of molecules containing fluorophores.

$$\text{Molecular Brightness, } \varepsilon = \frac{\sigma^2 - \langle k \rangle}{\langle k \rangle} \tag{5}$$

N&B analysis has several applications, such as studying the behaviour of proteins and their interactions in cellular membranes, investigating DNA-protein interactions and the dynamics of DNA molecules, and determining the distribution of oligomers within a sample when the brightness of a monomer is known. N&B analysis doesn't require sophisticated technical equipment, making it accessible to a wide range of researchers. It allows the calculation of the oligomeric states of proteins diffusing in cellular membranes when the brightness of a monomer is known. However, to the best of our knowledge, it has not yet been applied to study protein clustering, leading to pore formation.

1.6 Stepwise Photobleaching

This approach determines the aggregate stoichiometry of protein oligomers by digitally decreasing fluorescence intensity [76]. During imaging, the fluorophores of the fluorescently labeled sample undergo irreversible photobleaching after several excitation-emission cycles. This method can determine the number of fluorophores in a diffraction-limited area, such as within a protein oligomer. Photobleaching, being quantal, occurs in distinct steps; each bleaching event of an individual dye molecule is marked by a noticeable drop in the fluorescence intensity time trace of the complex (**Figure 8**). If each protomer in the complex is labeled with a single dye molecule (e.g., fusion constructs with green fluorescent protein (GFP)), the number of initial subunits in the complex can be directly inferred from the number of bleaching steps. To reduce intracellular background noise, this technique is often paired with total internal reflection fluorescence microscopy.

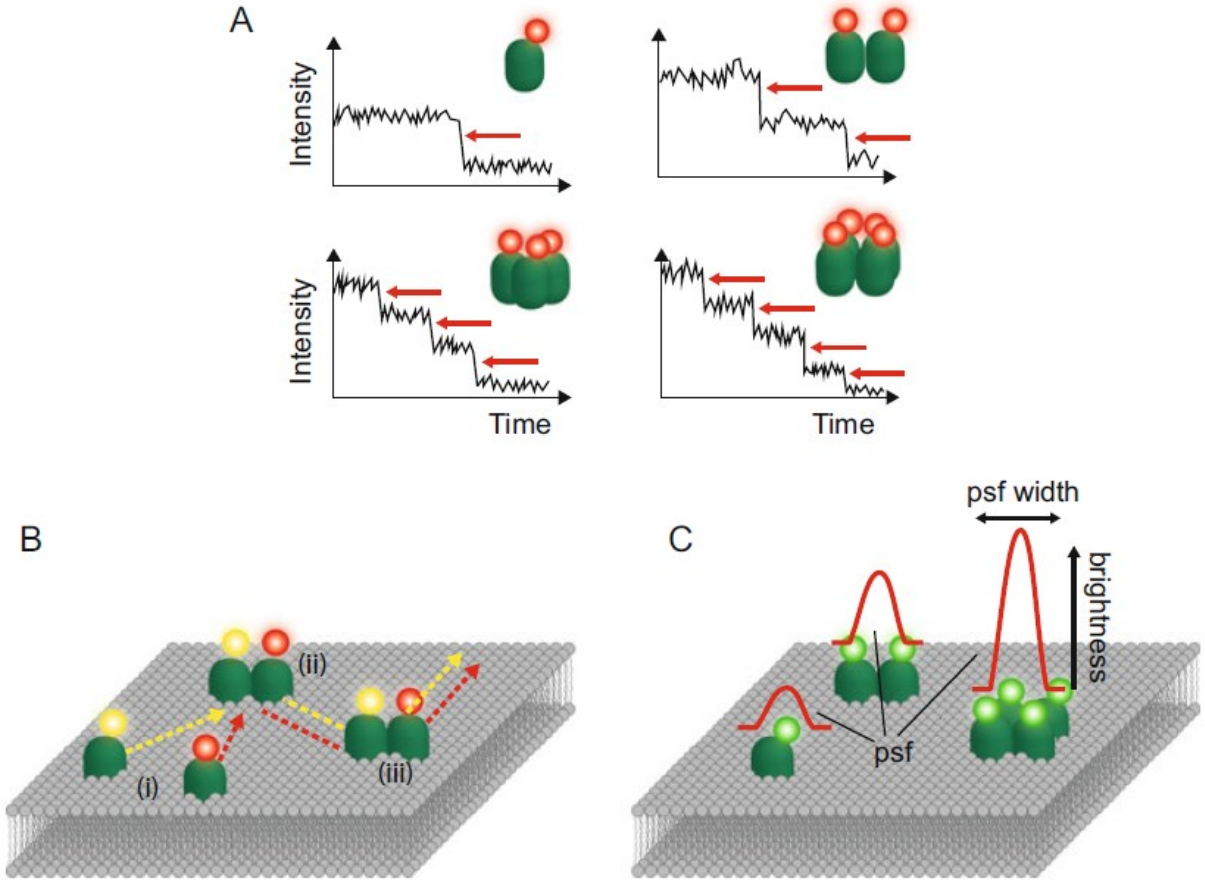

Figure 8: Stepwise photobleaching methods to determine protein oligomeric states. (a) Fluorescent intensity traces for mono, di, tri, and tetrameric proteins are shown. Each stepwise drop in the fluorescence intensity versus time plot corresponds to the photobleaching of one fluorophore. (b) Single Molecule Co-Tracking: The proteins of interest are labeled with

fluorophores of different spectra, and their diffusion paths in the membrane are tracked using localization algorithms. This allows direct visualization of molecular association (i), dissociation, and co-diffusion (ii and iii). (c) Fluorescent molecules are imaged based on their point spread function (PSF). Larger protein complexes do not produce a broader PSF compared to monomeric proteins, but they do exhibit a higher amplitude. Thus, analyzing the brightness of diffraction-limited spots enables the determination of the underlying oligomeric state. (The figure was adopted from "https://doi.org/10.1007/978-3-319-66601-3_8").

Overall, stepwise photobleaching is a powerful and precise method with a simple and direct readout for determining the oligomerization of membrane-bound proteins. Because this technique functions at the single-molecule level, it requires highly sophisticated and sensitive cameras. Despite the need for advanced equipment, the data analysis is straightforward and independent of assumed models. However, this method is limited to the analysis of immobile complexes. [77][78, 79].

1.7 Fluorescence Correlation Spectroscopy

Fluorescence correlation spectroscopy (FCS) is a highly sensitive and refined technique for detecting single molecules in motion. Originally introduced in 1974 by Elson and Magde, FCS was developed as a method for single-molecule detection, allowing for the study of the concentration, mobility, and interactions of fluorescence-labeled molecules [80]. This technique relies on analyzing the fluctuations in fluorescence intensity originating from the focal volume of a confocal microscope. As a fluorescent molecule diffuses through the focal volume, it becomes excited, and the resulting burst of emitted light is captured by highly sensitive detectors.

The fluorescence signal generated by repeatedly excited and emitted molecules as they diffuse through the detection volume is statistically analyzed. The fluctuations in time are described by the normalized autocorrelation function.

$$G(\tau) = \frac{\langle I(t) \cdot I(t+\tau) \rangle}{\langle I(t) \rangle^2} \quad (6)$$

In the eqn. 6, $I(t)$ represent the fluorescence intensity at time t, while τ refers to the lag time. The angle brackets denote time averaging. By fitting the autocorrelation function G(τ) to an

appropriate model, key parameters can be extracted, such as the diffusion time τ_D, which indicates how long a fluorophore remains within the focal volume, and the average number of fluorophores in the focal volume (denoted as (PN)). A two-dimensional model is employed when analyzing fluorophores within planar lipid bilayers [80] [Elson EL., Magde D]:

$$G(\tau) = 1 + \frac{1}{PN} + \frac{1}{1+\left(\frac{\tau}{\tau_D}\right)} \tag{7}$$

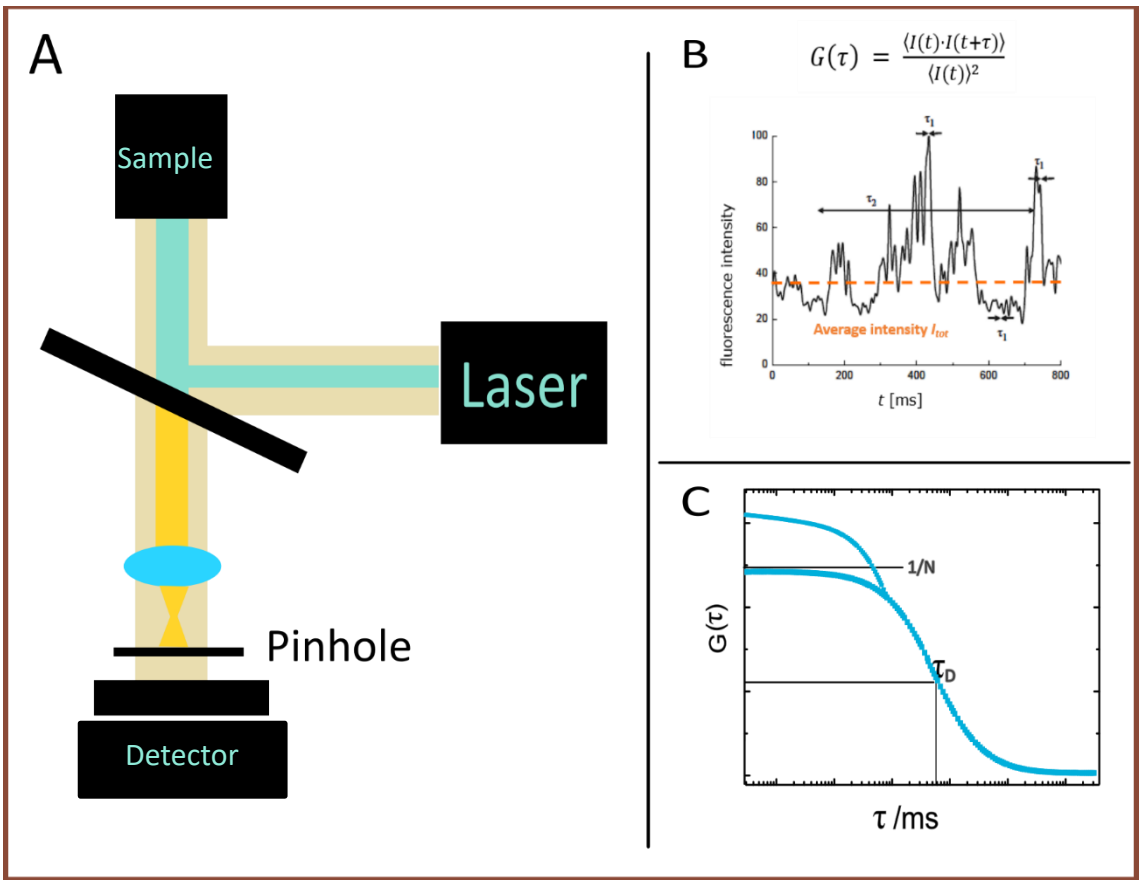

Figure 9: Principles of FCS measurements **(**A) A laser beam excites fluorescent particles as they diffuse within the detection volume. (**B)** The emission from these fluorophores leads to fluctuations in fluorescence intensity, which are recorded by a detector. (**C)** These intensity fluctuations are then correlated to produce an autocorrelation curve. The diffusion time τ_D is determined at the half maximum of the autocorrelation function.

The diffusion coefficient *D*, a key parameter for describing lateral diffusion, can be directly calculated from the diffusion time τ_D using the following equation:

$$D = \frac{\omega_0^2}{4\tau_D} \quad (8)$$

where ω_0 represents the radius of the detection volume. **Figure 9** illustrates the principle behind this method.

FCS's single-molecule sensitivity has made it popular across various research fields. Its most common application is in measuring the molecular diffusion and concentration of fluorescently labeled particles. Additionally, FCS can be used to measure kinetic rate constants of chemical reactions or other quantities that result in intensity fluctuations within the observed volume. However, the FCS method requires very low concentrations (nanomolar or picomolar) of fluorescent molecules because the optimal signal-to-noise ratio is achieved when, on average, only one fluorescent molecule is present within the detection volume.

Over time, scientists have adapted the classical FCS method to address increasingly complex problems. One such adaptation, brightness-FCS, has been further developed in this thesis to determine protein oligomeric states (see the Results section of this thesis). Other successful variants of FCS include Z-scan FCS and fluorescence cross-correlation spectroscopy [81].

1.8 Antibunching

Fluorescence antibunching is a less frequently used technique for determining the number of independent emitters per molecule or molecular complex. It was rarely applied to auto-fluorescent proteins due to the necessity of collecting large numbers of fluorescence photons from a single molecule, which is usually impossible to achieve with rather photolabile auto-fluorescent proteins. However, it can be well applied to molecules in solution, allowing us to accumulate data over a large number of molecules. It has been used to determine the average stoichiometry of molecular complexes. The proposed method is absolute in the sense that it does not need any calibration or referencing [82].

Photon antibunching is a phenomenon where a single photon emitter, such as a fluorescent molecule, cannot emit more than one photon at a time. Consequently, the probability of detecting photon pairs from a single molecule within a very short lag time between them approaches zero as the lag time itself approaches zero. This characteristic drop in probability is determined by the fluorescence lifetime of the molecule. If multiple molecules

are present, the drop does not reach zero but stabilizes at a higher value, which is determined by the number of independently fluorescing molecules within the detection volume. Therefore, antibunching can be used to determine the number of independently emitting molecules within a molecular complex, and this technique has been effectively applied to measurements of immobilized molecules [83]. However, a limitation of this method is the requirement for high photon count rates and photostable molecules to obtain reliable antibunching data. To address issues like photobleaching and low signal strength, one approach is to perform measurements in solution and accumulate signals from many molecules passing through the detection volume. Although antibunching measurements on fluorescent molecules diffusing in solution were first successfully demonstrated in 1985, this method has not been widely applied to determine the number of independently fluorescing molecules within a diffusing complex [84].

1.9 Förster resonance energy transfer

Förster resonance energy transfer (FRET) is most likely the most popular fluorescence method to study direct interactions of fluorescently tagged biomolecules [56, 85, 86] (**Figure 10**) in models as well as plasma membranes of living cells. Two types of molecules are used in this approach: the first type serves as the donors, and the other type serves as kaskacceptors of the excited energy. Dipole-dipole coupling between the donors and acceptors enables non-radiative energy transfer from the excited donor to the acceptor, leading to the quenching of donor fluorescence. The donor-acceptor separation at half-maximum transfer efficiency is defined as the Förster radius, whereby the efficiency of energy transfer is inversely related to the sixth power of the distance. The optimal distance between donors and acceptors ranges between 1 and 10 nm, implying that the formation of protein oligomers with both donors and acceptors localized in these oligomers results in increased FRET efficiency.

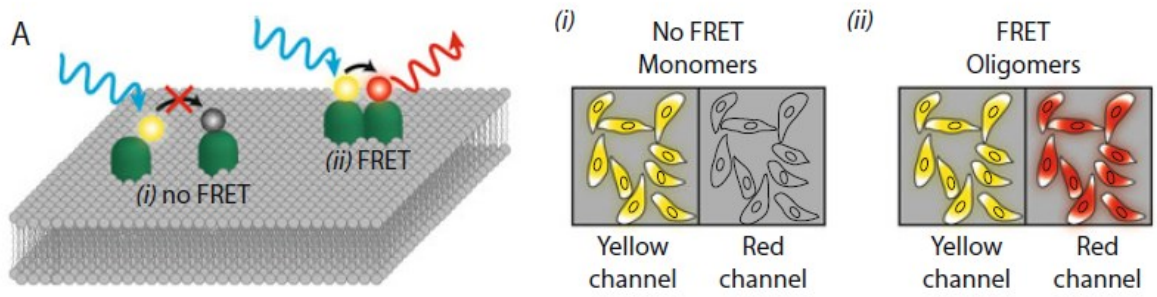

Figure 10: Förster resonance energy transfer method. Nonradiative energy transfer to the (red-shifted) acceptor dye molecule happens only when the two dyes are near to each other, as in an oligomer, after the donor dye molecule is excited. The rate of the energy transfer

depends strongly on the distance between the two dye molecules. (Figure was adapted from "https://doi.org/10.1007/978-3-319-66601-3_8").

A simplistic description of the mechanisms underlying FRET involves the energy transfer from an excited (donor, D^*) molecule to a neighboring (acceptor, A) molecule in its ground state via non-radiative dipole-dipole coupling of the two chromophores. The rate coefficient $\kappa_{FRET}^{D^*\to A}$ is dependent on the donor fluorescence lifetime (τ_D), the Förster radius (R_0) and the distance (r) that separates the two fluorophores.

$$\kappa_{FRET}^{D^*\to A} = \frac{1}{\tau_D}\left(\frac{R_0}{r}\right)^6 \tag{9}$$

FRET provides a direct way to display the interaction between two participants in the plasma membrane. A somewhat reliable readout is produced by the energy transfer's high dependency on the separation between the two dyes. Fluorescent proteins that are well-established and can be used in large quantities for genetic fusion to the target protein include cyan fluorescent protein (CFP) and yellow fluorescent protein (YFP). The precise number of subunits in the oligomer can be determined with Monte Carlo simulations, as recently shown in Škerle et al. 2020 [87]. The high correlation between the energy transfer and the distance between the dye molecules in an oligomer is a potential disadvantage of FRET; if the distance between the two dye molecules is too great, FRET will not be detected. Furthermore, even though there aren't any oligomers present, a discernible FRET signal could be produced by the stochastic proximity of dyes if the protein surface density is sufficiently high.

2. In-membrane Pore Formation by FGF2

2.1 FGF2 – An Overview

The discovery of fibroblast growth factor (FGF) protein dates back to 1973, when it was first identified in pituitary extracts[88]. FGFs are commonly found in various tissues and cells. Among them, FGF1 is often referred to as acidic FGF, while FGF2 is known as basic FGF. These growth factors were initially isolated from the brain and pituitary gland for their role in stimulating fibroblast growth.

Over time, researchers have identified and isolated at least 22 different distinct FGFs, each with its unique properties and functions [89, 90]. The basic fibroblast growth factor (bFGF) has a variety of functions in both physiological and pathological processes: Embryonic development, hematopoiesis, cell proliferation, cell differentiation, and wound healing are a few of the physiological processes where FGFs are crucial.

FGF2 is a versatile growth factor with a wide range of biological and physiological roles. It influences cell growth, differentiation, and signaling pathways in numerous contexts, including tissue development, repair, and maintenance. Its multifaceted functions make it a crucial player in normal physiological processes, and its dysregulation can have significant implications for various diseases, including cancer and neurodegenerative disorders [91, 92].

Understanding the role of FGF2 in these processes is essential for advancing our knowledge of biology and for the development of therapeutic strategies. With several tissue engineering applications being created and going through clinical trials, FGF2, in particular, is being studied as a possible therapeutic component for different illnesses and injuries, such as peripheral nerve damage. FGF2, as it encourages cell survival and angiogenesis, also plays a significant role in many forms of cancer. Due to this, FGF2 is also intriguing as a possible early indicator of tumour development or a target for cancer treatment[93].

2.2 FGF2 structure and stability

FGF2 appears to be a globular protein with a folded diameter of around 4 nm based on its crystal structure [94]. This protein is a β-tertiary structure with 12 antiparallel β strands joined by β turns. The protein surface is covered with many charged residues, whereas the barrel's centre is lined with hydrophobic residues. A bundle of positively charged residues to one side is believed to organize the heparin-binding site of the protein [95]. The receptor binding domain is also located in this area but is the same as the heparin-binding region. The accompanying image shows the globular structure of FGF2, highlighting its complex folding and active sites (see **Figure 11**).

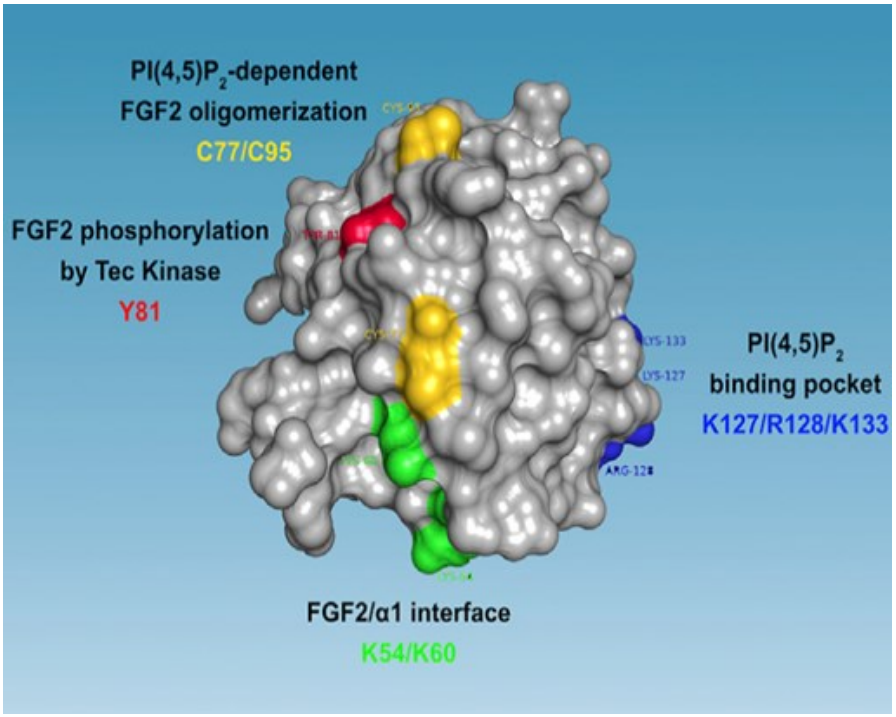

Figure 11: The structure of Fibroblast Growth Factor 2 (FGF2). (The figure was adopted from "doi: 10.3389/fcell.2022.864257")

The latent instability of FGF2 has been linked to the vital quantity of structural energy associated with the binding site of heparin and the binding ratio as low as 03:1 (heparin: FGF2) or with similar glucosaminoglycans [95–97]. In vivo, the interactions of FGF2 with molecules like heparin, heparin sulphate proteoglycan, and fibrin/fibrinogen present in soluble form or bound to cell membranes are understood to influence its stability, receptor reactions and concentration in an outer microenvironment of the cell [98].

2.3 Unveiling the mystery of FGF2 pores

Several different kinds of unconventional protein secretion (UPS) pathways carry a large number of proteins into the extracellular environment[99–102]. Although FGF2 must reach the extracellular space to activate FGF2 receptors on cell surfaces, its primary structure analysis showed it lacks a signal peptide necessary for ER/Golgi-dependent protein secretion. Despite significant efforts over the years, the hypothesis that alternative pathways for protein secretion exist remained speculative for decades[103, 104]. Only recently have detailed insights into the molecular mechanisms by which FGF2 and other UPS cargoes are transported into the extracellular space been discovered[99–102, 105].

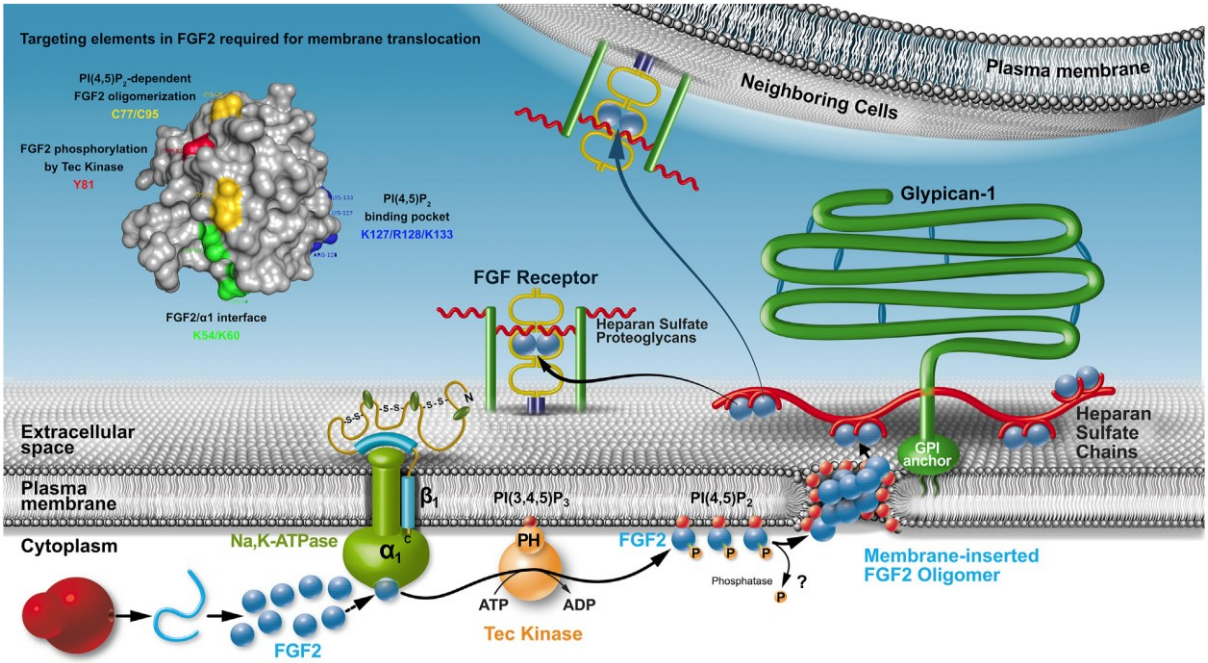

Figure 12: Unconventional protein secretion I pathway of FGF2 for bypassing the use of intracellular vesicle intermediates. Instead, it directly translocates across the plasma membrane. This figure includes all the steps in the translocation process. (The figure was adopted from "doi: 10.3389/fcell.2022.864257")

All components (Na, K-ATPase[106, 107], PI(4,5)P2 membrane[108–110], Tec kinase[111–113] of the molecular machinery responsible for the unconventional secretion of FGF2 have been found to be localized at the plasma membrane (**Figure 12**). An assemble of amino acids (K127, R128, and K133; **Figure 12**) with basic side chains facilitates PI(4,5)P2 supported membrane binding of FGF2[69, 109, 114]. This interaction between PI(4,5)P2 starts the core mechanism of FGF2 protein membrane translocation, a process that involves

membrane insertion of FGF2 oligomers[69, 105, 112]. The formation of these oligomers relies on intermolecular disulfide bridges[69, 99, 114]. As depicted in the figure above, the membrane pore induced by FGF2 oligomers features a toroidal architecture[105, 112, 114].

Several experimental observations back this perspective, such as the concurrent membrane passage of fluorescent tracers and the trans-bilayer diffusion of membrane lipids, which occur alongside the PI(4,5)P2-dependent membrane insertion of FGF2 oligomers[105, 112]. Additionally, diacylglycerol, a cone-shaped lipid that interferes with the positive membrane curvature induced by PI(4,5)P2, prevents the formation of membrane pores by FGF2 oligomers[105, 112]. Consequently, PI (4,5)P2 is involved in the secretion of FGF2 in three different ways: 1) mediating the binding of FGF2, 2) starting FGF2 oligomerization (in-) membrane, and 3) maintaining positive membrane curvature to cause the lipid bilayer to change into a toroidal membrane pore that can accommodate membrane-inserted FGF2 oligomers in its hydrophilic centre[99, 105].

As a result of FGF2's ability to bind multiple PI(4,5)P2 molecules, it is hypothesised that a strong local accumulation of this bilayer perturbing membrane lipid could impact the integrity of the plasma membrane and aid in the process of membrane remodelling, which would transform the lipid bilayer into a toroidal membrane pore[69, 99, 100]. Membrane-inserted FGF2 oligomers are thought to constitute membrane translocation intermediates as part of an assembly/disassembly route that propels the directed transport of FGF2 into the extracellular space, based on the findings previously presented [99, 105].

Heparan sulphate proteoglycans on the cell surface mediate the last stage of this process, which involves capturing FGF2 at the plasma membrane's outer leaflet[115–118]. Of note, heparan sulphates have an approximately 100-fold greater affinity for FGF2 than PI(4,5)P2[69, 108, 109, 119]. Additionally, the binding sites of heparan sulphates and PI(4,5)P2 in FGF2 overlap with certain important residues, such as K133, which is necessary for both kinds of interactions[69, 108, 109]. It is consistently demonstrated that FGF2's interactions with PI(4,5)P2 and heparan sulphate chains are mutually exclusive[69]. These results provide a convincing explanation of how FGF2 assembles at the inner leaflet in a PI(4,5)P2-dependent manner into membrane-inserted oligomers that are captured and disassembled at the outer leaflet by cell surface heparan sulphate chains. They also reveal a crucial component of the molecular mechanism of FGF2 membrane translocation[99, 100,

102]. Therefore, FGF2 is maintained on cell surfaces, and heparan sulphates promote the final stage of FGF2 membrane translocation (**Figure 12**).

FGF2 can spread to nearby cells after translocation into the extracellular space. This is most likely due to the direct exchange between heparan sulphate chains that are connected to proteoglycans on adjacent cell surfaces[116]. Heparan sulphate proteoglycans, thus, perform a variety of roles from the production of FGF2 on free ribosomes to the cell surface, with the first being the mediation of the last stage of FGF2 secretion[115, 116], 2) protection of FGF2 on the extracellular region of cell surfaces against denaturation and degradation[120] and 3) triggering the FGF2 signalling through ternary complexes in which heparan sulfate chains and FGF high-affinity receptors are involved[121–123].

To summarise, the process of directed transport of FGF2 into the extracellular space is reliant on the sequential connections between FGF2 and PI(4,5)P2 at the inner leaflet, as well as interactions with heparan sulphates on the cell surface through bridging membrane translocation intermediates (**Figure 12**). Previous research showing that FGF2 stays in a fully folded state during every stage of its unusual secretory route lends additional credence to the hypothesised mechanism[110, 124, 125], a phenomenon that reflects the requirement for the formation of defined oligomers during membrane insertion. These findings imply a quality control step that ensures secretion to be limited to FGF2 species that are biologically active[110, 124].

One potential component of the FGF2 unconventional secretory pathway that pertains to quality control is the involvement of Na, K-ATPase. On the other hand, its role might be limited to constructing a landing platform at the inner plasma membrane leaflet to serve as FGF2's initial point of contact[107]. It is also hypothesised that the control of the Na,K-ATPase's ATPase activity may be connected to the aberrant production of FGF2[100]. Because FGF2 binds to a location in the cytoplasmic domain of the α-subunit of the Na,K-ATPase that includes its enzymatic activity, and because FGF2 secretion entails the development of a brief lipidic pore in the plasma membrane[107]. The idea that FGF2 could increase this Na,K exchanger's ATPase activity seems like a fascinating theory. Consequently, in situations where lipidic membrane pores are formed during FGF2 unconventional secretion—a process that doesn't seem to threaten cell viability—this could aid in maintaining the membrane katsinpotential[99, 100, 105].

Interestingly, the schematic representation in **Figure 12** shows a molecular mechanism that is also applicable to other protein secretions, like HIV-Tat and tau protein. Similar to FGF2, both mechanisms necessitate direct physical contact with the plasma membrane's inner leaflet, PI(4,5)P2, and outer leaflet, heparan sulphates[126–131].

Research objective

The major objective of this work is to contribute to an enhanced understanding of FGF2 pore formation in biological membranes. For this purpose, we developed a new single-molecule fluorescence method, dual-(+1)-FCS, which enables to correlate membrane pore formation with protein oligomerization, thus providing an improved insight into the mechanism by which FGF2 is translocated over the lipid membrane. For better understanding, this work is divided into two methodological parts:

Part I: Development of a functional assay to correlate protein oligomerization states with membrane pore formation.

In addressing the challenge of distinguishing functional oligomers from irrelevant aggregates, we focus in this section on the development of a statistical fluorescence assay utilizing single molecules and single giant liposomes. The method evaluates the brightness of individually diffusing in-membrane oligomers and establishes a correlation between their oligomerization state and the formation of membrane pores. It also enables the analysis in a time-dependent manner, allowing for the monitoring of the formation of membrane pores as a function of time.

Part II: Determining the functional oligomeric state of membrane-associated FGF2 oligomers forming membrane pores on giant lipid vesicles.

In Result Part II, we use the developed assay on the specific case of FGF2 with the aim to identify the functional oligomeric state of FGF2 during the transient formation of membrane pores. With this approach, we could distinguish between functional oligomers of FGF2 and non-specifically aggregated proteins lacking functionality. Specifically, we observed two distinct populations of FGF2: (i) dimers to hexamers and (ii) a diverse population of higher oligomeric states of membrane-associated protein oligomers. This diversity markedly distorted the original unfiltered histogram, encompassing all detectable oligomeric species of FGF2.

3. Part I: Development of “dual-(+1)-FCS” approach

Despite significant technological advancements, a considerable limitation of available high-resolution microscopy methods is their inability to distinguish between functional and dysfunctional protein aggregates within the membrane. This implies that while available microscopy techniques can provide high-resolution information about the oligomerization degree of proteins, they can no longer determine whether the detected oligomeric unit is also functional. Meanwhile, only functional aggregates are essential for normal cellular operations, such as forming functional ion channels or signalling complexes. In contrast, dysfunctional aggregates can lead to pathological conditions, or they simply have no biological function at all. The inability to differentiate between these states can hinder the interpretation of experimental data and the understanding of underlying mechanisms in both health and disease.

To overcome these limitations, there is a need for the development of new methodologies to enhance their specificity and sensitivity. This may involve combining multiple methods to cross-validate findings, or also combine advanced computational simulations with experimental techniques, or developing new labelling strategies that can differentiate the functional states of protein aggregates. Such advancements would be more crucial for gaining a more comprehensive and accurate understanding of the complex interplay between proteins associated with membranes[79, 132–134].

In this context, we present here a versatile single-vesicle fluorescence technique, enabling the quantification of protein oligomeric states undergoing self-assembly on free-standing model lipid membranes and correlating the determined average oligomeric state on a single GUV to GUV permeability. By executing these experiments on an ensemble of GUVs and in a time-dependent fashion, we could establish a correlation between in-membrane protein oligomerization and the development of functional in-membrane pores.

3.1 Mysterious '(+1)' in dual-(+1)-FCS

The new method, called dual-(+1)-FCS, employs three distinct detection emission channels using three different fluorescent dyes. This contrasts with the classical two-color FCS (dual-FCS), which uses only two channels. In our experimental design, we utilized two emission channels for classical dual-colour FCS [80] and used the third emission channel to monitor membrane permeabilization via the in-leakage of a fluorescent dye (**Figure 13**). Specifically, we labelled the GUV membrane with a lipid analogue probe DOPE-Atto-633 (excitation wavelength is 629 nm and emission wavelength is 657 nm). This allowed us to label all GUVs, including those without any membrane-associated FGF2 protein, and to perform a quality check on the membrane. The second emission channel was then reserved for the pore-forming protein FGF2 labeled by the Green Fluorescent Protein (FGF2-GFP, the excitation wavelength is 488 nm, and the emission wavelength is 510 nm). In this case, to follow the in-membrane oligomerization of FGF2, we used FCS and calculated the brightness and diffusion coefficient of FGF2 in the membrane (see the section below).

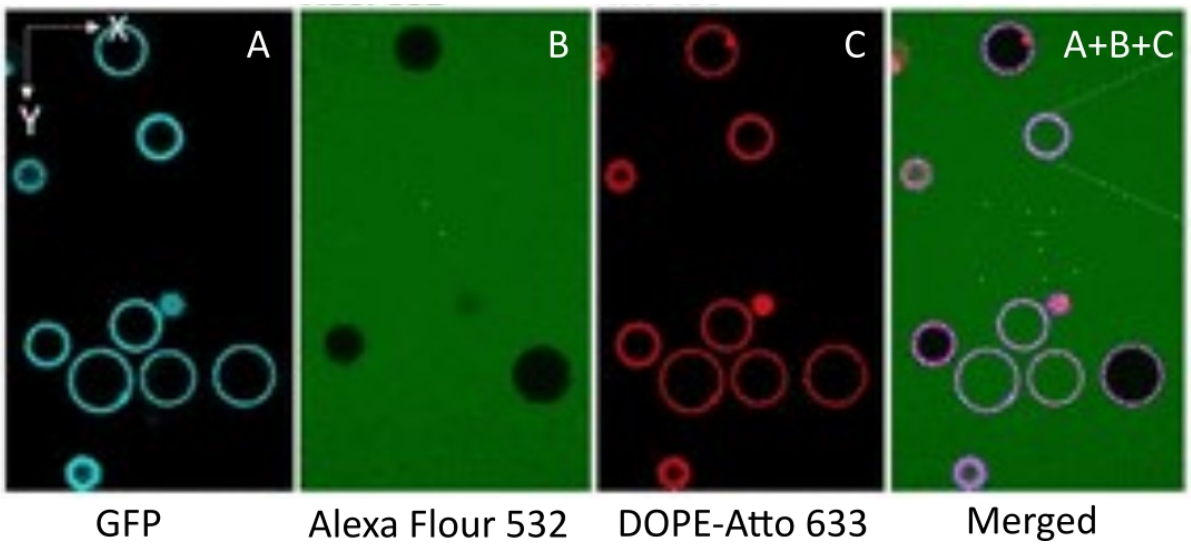

Figure 13: (A) FGF2-GFP associated with the GUV membrane, (B) Alexa-Fluor-532 probing GUV membrane permeability, (C) GUV membrane labeled with DOPE-Atto-633, and panel (A+B+C) is the merged image of all three fluorescent dyes.

To monitor GUV membrane permeabilization and differentiate between leaky GUVs (containing membrane pores) and non-leaky GUVs (intact membranes), we used the third emission channel and the dye Alexa-Fluor-532 (excitation 532 nm, emission 590/50nm) as a 'background' dye. Leaky GUVs were identified by an increased intensity of Alexa-Fluor-532

inside the GUV. In contrast, non-leaky GUVs remained intact with minimal background dye content inside. More specifically, leaky GUVs were characterized by an Alexa-Fluor-532 intensity exceeding 20%, while non-leaky GUVs had an Alexa-Fluor-532 concentration below 20% (**Figure 13**).

3.2 Calculation of readout dual-(+1)-FCS parameters

The dual-(+1)-FCS method involves four steps to determine all necessary readout parameters. In Step I, leaky and non-leaky GUVs are distinguished and selected. A GUV is classified as leaky or non-leaky using Alexa-Fluor-532 (excitation 532 nm, emission 590/50 nm). In the second step, a membrane is positioned within the focal region of 470 nm and 635 nm lasers. Subsequently, a series of dual-colour fluorescence correlation spectroscopy FCS measurements, each lasting 60 seconds, is conducted using emission channels of 515/50 nm (FGF2-GFP) and 697/58 nm (DOPE-Atto-633). The resulting auto-correlation (AC) curves undergo fitting utilising a model that postulates two-dimensional diffusion within the membrane (FGF2-GFP and DOPE-Atto-633), three-dimensional diffusion in the solution (FGF2-GFP in bulk), and the dye transitioning to the triplet state [135].

$$G(\tau) = 1 + \left(\frac{1}{N} \frac{1}{1 + \left(\frac{\tau}{\tau_D}\right)} + \frac{1}{N_{\text{free}}} \frac{1}{1 + \left(\frac{\tau}{\tau_{D,\text{free}}}\right)\sqrt{1 + SP\frac{\tau}{\tau_{D,\text{free}}}}} \right) \frac{1 - T + T\, exp\left(-\frac{\tau}{\tau_T}\right)}{1 - T} \qquad (10)$$

In this context, τ represents the lag-time, τ_D denotes the diffusion times of the membrane-bound dye, *SP* indicates the structure parameter, *T* signifies the fraction of the dye in the triplet state, and τ_T represents the lifetime of the triplet state. Within the central beam region, the fluorescent signal originating from the solution is negligible; consequently, the above equation can be simplified to:

$$G(\tau) = 1 + \frac{1}{N} \frac{1}{1 + \left(\frac{\tau}{\tau_D}\right)} \frac{1 - T + T\, exp\left(-\frac{\tau}{\tau_T}\right)}{1 - T} \qquad (11)$$

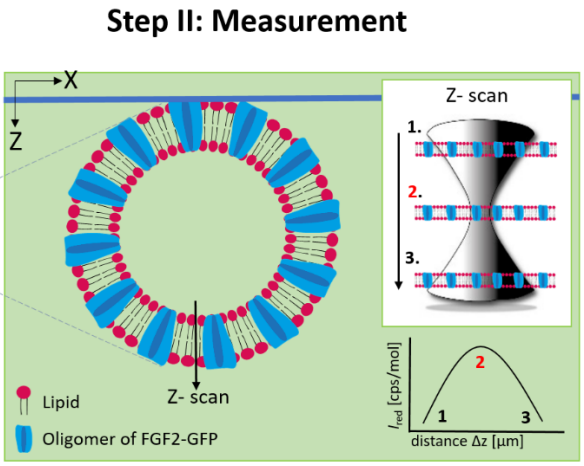

Figure 14: dual-color Fluorescence Correlation Spectroscopy on a single GUV involves focusing the bilayer into the beam center. The measurement begins by aligning the bilayer using the maximum red signal along the black arrow in the vertical XZ GUV plane. The correct membrane position, where the bilayer is optimally focused, is marked as "2".

In step II, single GUVs are measured using dual-(+1)-FCS. The process begins with precisely aligning the bilayer within the central area of the focal volume. This alignment is achieved by identifying the peak intensity in the red signal, as indicated by the black arrow in **Figure 14**, within the vertical XZ plane of the GUV. Subsequently, the accurate position of the membrane is annotated as '2' to ensure proper alignment. Particularly, in this method, it is imperative to measure all output parameters under conditions where the membrane is precisely aligned with the centre of the beam. If that is not the case, inconsistent results will be obtained.

In Step III, the mean intensity for both the monomer $\langle I(\text{mono})\rangle$ and the oligomer $\langle I(\text{oligo})\rangle$ is determined as outlined in **Figure 15,** and a fitting analysis of the autocorrelation functions $G(\tau)$ for the monomer, oligomer, and the lipid tracer DOPE-Atto-633 is performed. The resulting fits provide essential output parameters: the quantity of independently diffusing oligomers/monomers $N(\text{oligo/mono})$ within the confocal volume, along with their respective diffusion times (see Eq. 12,13).

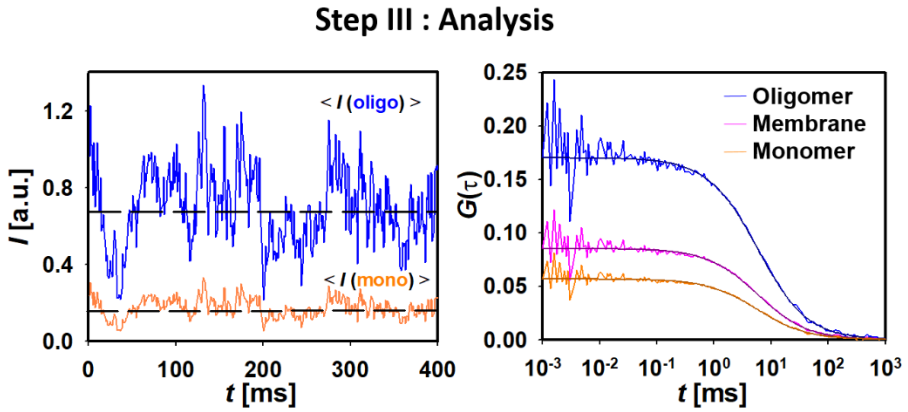

Figure 15: The dual-(+1)-FCS analysis includes (A) calculating the average intensity for the monomer (<*I*(mono)>) and the oligomer (<*I*(oligo)>), as well as fitting the autocorrelation functions *G*(τ) for the monomer, oligomer, and the lipid tracer DOPE-Atto-633. (B) The fitting process provides the readout parameters mentioned in the text.

In the last step, the average oligomeric state on a single GUV is determined based on a comparison of the brightness of an oligomer ϕ(oligo) to that of a monomer ϕ(mono). The brightness of an oligomer is calculated as ϕ(oligo) = *I*(oligo)/*N*(oligo), where <*I*(oligo)> represents the average intensity, and *N*(oligo) denotes the number of molecules in the focal volume. The brightness of a monomer ϕ(mono) is obtained in a similar manner as ϕ(oligo), but it needs to be ensured that the probability that two labelled protein molecules meet in a cluster is negligible.

Finally, the average oligomeric state *N*(m.u.) is calculated as:

$$N(m.u.) = \frac{\phi(\text{oligo})}{\phi(\text{mono})} \tag{12}$$

The diffusion coefficient *D* of GFP and DOPE-Atto-633 is determined by using the following relationship:

$$D = \frac{\omega^2}{4\tau_D} \tag{13}$$

Here, ω denotes the radial distance from the optical axis, corresponding to the points where the intensity has attenuated to $1/e^2$. The size of the volume element can be calculated by analyzing a 5 nM aqueous solution of rhodamine 6G, which has a known diffusion coefficient $D = 2.8 \times 10^{-8}\, m^2/s$ [136].

Finally, protein surface concentration (PSC) was calculated as the number of protein molecules in the confocal spot *N*(oligo/mono) **N*(m.u.) of a known radius ω:

$$\mathrm{PSC} = \frac{N(m.u.) \times N(\mathrm{oligo/mono})}{\pi \omega^2} \quad (14)$$

3.3 Work-flow of a typical dual-(+1)-FCS measurement

A dual-(+1)-FCS was performed on an Olympus FluoView 1000 MPE system, which was upgraded with a dual detector channel PicoQuant laser scanning microscope (LSM) Upgrade Kit. Additionally, a homebuilt excitation system was integrated, comprising LDH-D-C-470 and LDH-D-C-640 diode laser heads, along with 543nm He-Ne continuum wave lasers.

A typical dual-(+1)-FCS measurement starts by imaging individual GUVs using FluoView software in conjunction with conventional FluoView 1000 hardware. The GUVs are classified as either leaky or non-leaky based on predefined criteria (see above). In the case of a time-resolved measurement, the position coordinates of each GUV are stored in memory, enabling repeated dual-(+1)-FCS measurements on a selected set of GUVs. Once a GUVs is selected, the laser beam is precisely positioned onto the GUV membrane. The emission from the membrane is collected using a HydraHarp400 Multichannel Picosecond Event Timer and time-correlated single photon counter (TCSPC) module, controlled via SymPhoTime64 software. The software also facilitates control of the pulse diode laser (PDL) 828 Sepia II driver (PicoQuant, Berlin, Germany).

The emission signal collected from the GUV membrane is then correlated, and autocorrelation curves are obtained. These AC curves are subsequently fitted by a model assuming two-dimensional diffusion in the membrane and dye transition to the triplet state (Eq 10). This fitting process allowed for the extraction of crucial FCS output parameters, including the average protein oligomeric state and the protein surface concentration of FGF2 on each selected GUV, as well as the diffusion coefficient (see the section above). Overall, the microscopy setup and measurement protocol described herein provides a robust and comprehensive approach for investigating membrane pore formation at the single-vesicle level.

3.4 Methodology of Time-Resolved dual-(+1)-FCS measurements

As illustrated in Singh et al. 2023 [137], a dual-(+1)-FCS measurement can also be performed in a time-resolved manner by following individual GUVs in time and monitoring protein oligomerization and membrane permeability as a function of time. Consequently, in our analysis, we classified single GUVs not only based on their permeability in ONE state but in at least two consecutive states: in the FINAL state that has reached equilibrium and in the INITIAL state, usually characterized shortly after the incubation of the protein with the GUVs. Based on the history of the FGF2 pores, this classification resulted in four distinct GUV categories (**Figure 16**):

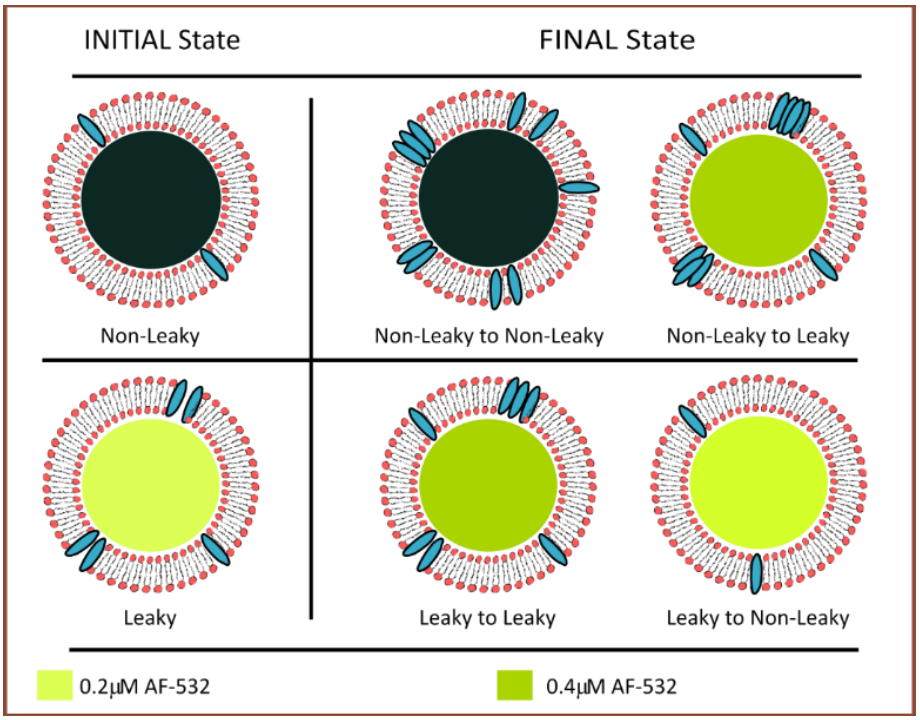

Figure 16: The GUVs shown on the left-hand side of the figure represent the GUVs in the INITIAL state. They can be either leaky or non-leaky, as monitored by the in-leakage of Alexa-Fluor-532. The right-hand side of the figure represents the GUVs in the FINAL state 240 minutes after the incubation of FGF2 with the GUVs. As shown in the figure, four different cases are possible and can be distinguished from each other by adding a new aliquot of Alexa-Fluor-532.

1. leaky → leaky: GUVs with continuously open pores between the INITIAL and FINAL states.

2. non-leaky → non-leaky: GUVs with impermeable membrane in both the INITIAL and FINAL states.

3. non-leaky → leaky: GUVs that transit from the non-leaky to leaky state between the INITIAL and FINAL measurements.

4. leaky → non-leaky: GUVs where the pores close after the INITIAL measurement.

The main aim of this work was then to determine to what extent the oligomerization degree of FGF2 varied between the distinct membrane permeabilization states and whether it evolved over time.

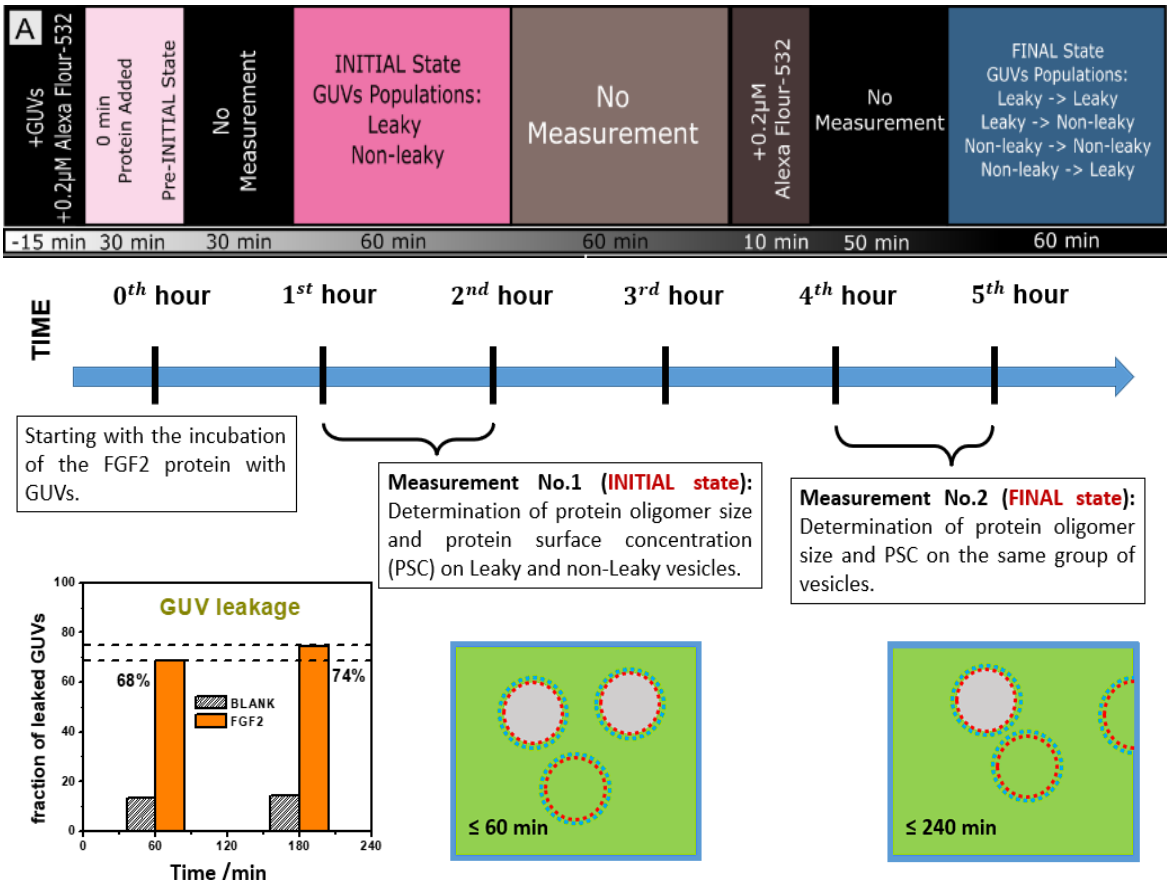

Figure 17: The time-course of a time-resolved dual-(+1)-FCS measurement. The whole measurement takes about 315 minutes.

A typical design of a time-resolved dual-(+1)-FCS experiment is outlined in **Figure 17.** To initiate the experiment, we immobilized GUVs within an IBIDI imaging chamber, and, subsequent to their introduction, they were introduced into a buffer solution containing Alexa-Fluor-532. The experimental procedure was followed with the introduction of the protein,

followed by an incubation period of at least 60 minutes, during which the GUVs were exposed to the FGF2 protein. Subsequently, dual-(+1)-FCS measurements were performed within the time frame of 1st to 2nd hour from the onset of the experiment, defining this phase as the INITIAL state. Between the 4^{th} and 5^{th} hour, a second dual-(+1)-FCS was performed, known as the FINAL state.

3.5 Advantages and disadvantages of dual-(+1)-FCS

The advances in single-molecule and super-resolution fluorescence microscopy opened new possibilities to accurately determine in-membrane protein oligomerization numbers. STED or single molecule TIRF microscopy, classified as true single-molecule approaches, appears to be the method of choice as it provides oligomer size distributions (i.e. histograms) of individual protein oligomers. They also have a realistic potential to resolve the molecular structure of these oligomer units in the membranes of native cells. However, these single-molecule methods, which are commonly applied to supported lipid bilayers, reveal broad distributions of oligomerization numbers of the investigated membrane proteins, whereby it is unclear whether all detected protein oligomers are functional. Attempts to reconstitute mobile membrane proteins in SPBs usually fail, as do many attempts to prepare SPBs with minimal effect of the support on in-membrane diffusion. These approaches have recently included the preparation of tethered and cushion SPBs and were only partially successful.

The possibility to apply dual-(+1)-FCS to GUVs has two significant advantages over single molecule and super-resolution fluorescence microscopy on SPBs: (1) the unique possibility to relate N(m.u.), D, and PSC(FGF2-GFP) to membrane permeability in one experiment, i.e. to link protein oligomerization to a functional readout, in this case, membrane pore formation. (2) The method enables measurements on free-standing membrane parts of GUVs, i.e. it enables measurement under natural conditions where the protein dynamics are not impeded by the underlying membrane support. Furthermore, since FCS is not a classical single-molecule approach, it can be used at relatively high surface concentrations of 1 nmol/m^2 or higher, where classical single-molecule approaches would fail (for comparison, 1 molecule in a confocal spot with a radius of 250 nm yields PSC = 9 pmol/m^2).

As the main limitation of dual-(+1)-FCS can be considered the fact that it yields the average oligomer size per single GUV, i.e. it does not provide a distribution of single oligomer species as the true single-molecule techniques do. Furthermore, as for any fluorescent

approach, achieving specific and full labeling of molecules with fluorophores is critical for the accurate determination of the oligomer size. Additionally, applying dual-(+1)-FCS to plasma membranes or living cells presents additional challenges due to cellular heterogeneity or photobleaching.

4. Part II: In-membrane oligomerization of FGF2 leading to membrane pore formation

To demonstrate the applicability of dual-(+1)-FCS, we studied the translocation of FGF2 across the plasma membrane, which involves the formation of membrane pores. We hypothesized that FGF2 pores form when the protein successfully inserts into the membrane, creating a defect that the bilayer cannot compensate for. Therefore, the presence of membrane pores indicates that the protein is functional and capable of being translocated across the plasma membrane.

We initiated the study by characterizing GUV membrane permeability in the INITIAL and FINAL states (see the section " Methodology of Time-Resolved dual-(+1)-FCS measurements" for the specific design of the experiment).

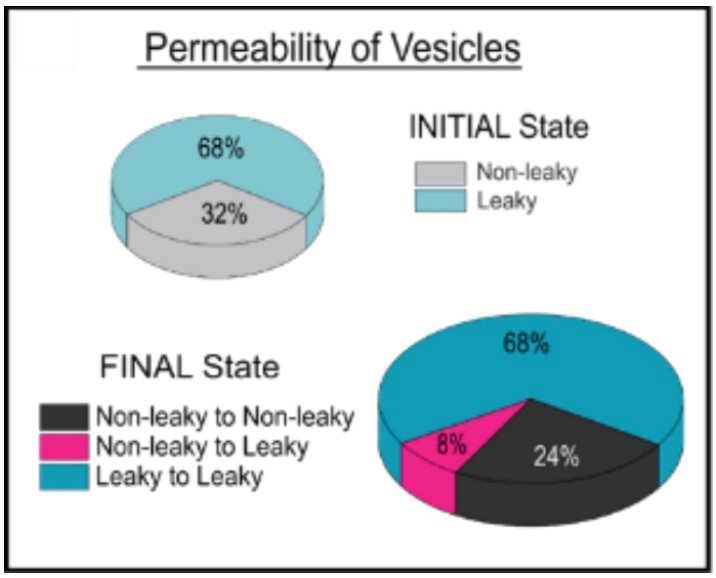

Figure 18: This pie chart shows that while FGF2 binds to the membrane of most GUVs during a 4-hour incubation period, some GUVs develop pores (become leaky), while others remain intact (non-leaky).

Here, **Figure 18** shows that 68 ± 3% of GUVs were observed to be leaky 60 min after the addition of the protein. This state is defined as the INITIAL state. At t = 180 min, a further fluorescence tracer was introduced to assess permeabilization in the FINAL state. The FINAL state, representing equilibrium ($t \geq 240$ min), revealed that 24 ± 1% of all GUVs remained intact. Consequently, the fraction of leaky vesicles increased by only 8 ± 1%, indicating a shift

from non-leaky to leaky GUVs. Particularly, a control sample lacking protein exhibited a leakage of 12 ± 1% in the INITIAL state and 14 ± 2% in the FINAL state, suggesting a baseline level of leakage.

4.1 Correlating FGF2 oligomeric state to membrane pore formation for the FINAL equilibrium state

In the next step, we used dual-(+1)-FCS to investigate the FGF2 oligomeric state and membrane permeability in the FINAL equilibrium state. **Figure 19** shows that the distribution of average oligomer sizes for the entire ensemble of 60 investigated GUVs is clearly bimodal, with peaks around N(m.u.) ≈ 4 and N(m.u.) ≈ 8.

Subsequently, we categorized GUVs into non-leaky and leaky GUVs based on membrane permeability after incubation with the protein. Additionally, plots for a double cysteine mutant (His-FGF2-C77/95A-GFP), where oligomerization was inhibited, are provided in the same figure. As demonstrated in **Figure 19**, leaky vesicles exhibit a significantly larger oligomer size, with a median value centred at median [N(m.u.)] = 7.4, compared to non-leaky vesicles with median [N(m.u.)] = 4.6. This correlation of oligomeric size with membrane permeability thus reveals two distinct populations of FGF2-GFP: one with a median [N(m.u.)] = 7.4, capable of permeabilizing the membrane, and another with a median [N(m.u.)] = 4.6, lacking this ability. Essentially, a control experiment using a mutant of FGF2, where oligomerization was disabled, yields a median [N(m.u.)] = 1.1. These results underscore the ability of dual-(+1)-FCS to unravel specific protein subpopulations that could not have been revealed with classical single-molecule approaches limited to supported phospholipid bilayers[69].

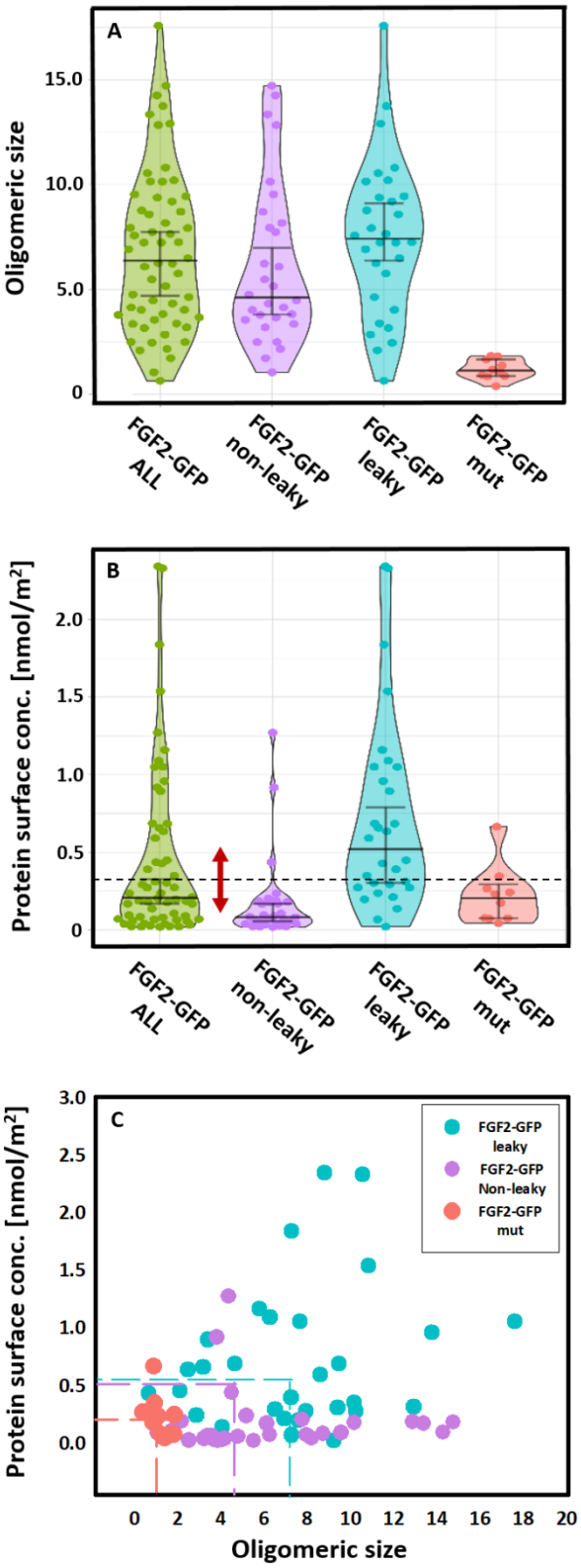

Figure 19: This figure illustrates the functional correlation between various parameters related to FGF2-GFP induced membrane pore formation. Panel (A) shows the oligomeric size of FGF2-GFP (*N*(m.u.)). The size of these oligomers, indicated by the number of molecules

forming a complex on the membrane, is represented by each dot, which corresponds to a measurement taken from a single GUV. Panel (B) depicts the surface concentration of FGF2-GFP (PSC(FGF2-GFP)) on the GUV membrane, measured in nmol/m². A threshold concentration is marked by a dashed line with a red arrow, indicating the upper limit of the concentration range (0 to 0.3 nmol/m²) reached by 90% of nonleaky GUVs. Panel (C) presents a 2D scatter plot that simultaneously displays the correlation between oligomeric size and surface concentration. Median values and 95% confidence intervals are shown by solid black lines in panels A and B, while colored dashed lines represent median values in panel C.

4.2 Correlating FGF2 Oligomeric State with Membrane Pore Formation in a Time-Resolved Manner

The experimental design can be further improved to observe changes in the FGF2 oligomeric state and membrane pore formation over time. We achieved that by measuring the *N*(m.u.) on the same GUV over the course of time. To illustrate this approach, *N*(m.u.) was estimated twice in the INITIAL state ($t = 0$ hrs) and subsequently at the end of the incubation period corresponding to the FINAL state ($t \geq 4$ hrs) (**Figure 20**).

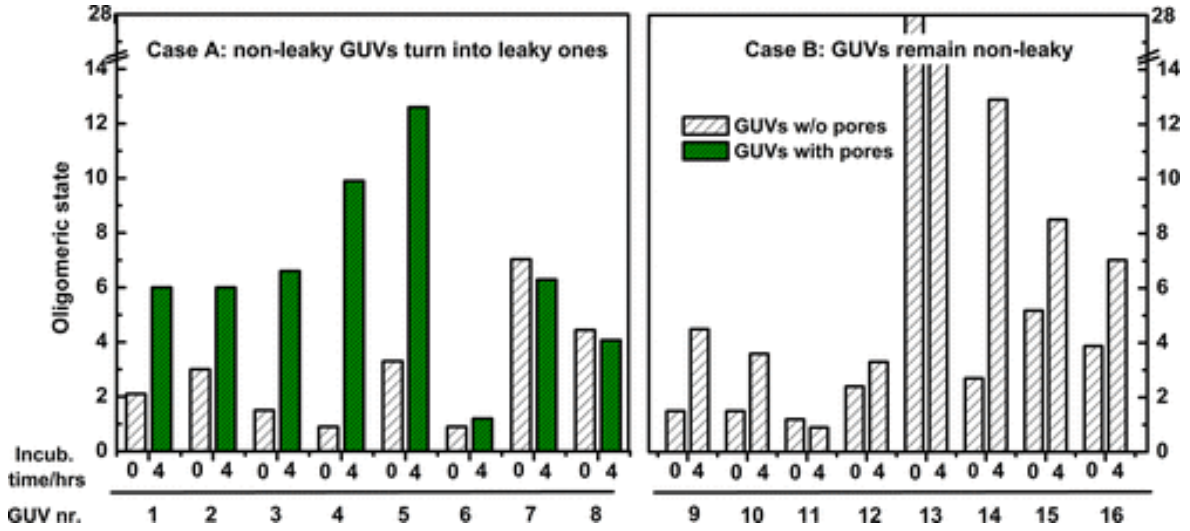

Figure 20: The correlation between the oligomeric size of FGF2-GFP and lipid pore formation was monitored over time on individual GUVs. (Case A) illustrates GUVs that initially did not allow the fluorescent tracer to penetrate (GUVs without pores) but became filled with the tracer during incubation with FGF2-GFP (GUVs with pores). In contrast, Case B displays GUVs that remained impermeable to the small fluorescent tracer throughout the entire experiment.

In panel A of **Figure 20**, GUVs that were not penetrated by the fluorescent tracer (GUVs w/o pores) at the start and subsequently were filled with the tracer during incubation with FGF2-GFP (GUVs with pores) are shown. Conversely, panel B illustrates GUVs that remained unpenetrated by the tracer throughout the experiment. Analysis of the data reveals that in 5 out of 8 cases, penetration of GUVs is accompanied by a significant increase in *N*(m.u.), indicating an increase in the oligomeric size as FGF2 pores are formed. Specifically, the average *N*(m.u.) for GUVs without pores at t = 0 hrs increased from 3.2 ± 2.07 to 7.4 ± 2.89 for GUVs with pores at $t \geq 4$ hrs. Conversely, among the 4 out of 8 vesicles that remained intact, there was a minor increase in *N*(m.u.) from 1.7 ± 0.52 at $t = 0$ hrs to 3.1 ± 1.54 at $t \geq 4$ hrs, which were significantly lower than the former case. Moreover, the FCS-based approach identifies individual GUVs that deviate from these trends. For example, GUV nr. 6 likely experiences non-specific leakage, as evidenced by a non-specific leakage rate of 17.9% among an ensemble of 16 GUVs. Conversely, GUVs nr. 13 to 16 do not exhibit leakage despite a high final *N*(m.u.), possibly due to non-functional protein aggregation at the membrane surface.

4.3 Correlating FGF2 protein oligomerization with pore formation

To shed more light on the time evolution of FGF2 membrane pore formation, indicative of the successful incorporation of the protein into the membrane, we significantly expanded the set of analyzed GUVs originally shown in **Figure 20** and presented in *Sachl et al.* [138]. After collecting the data from a total of 67 GUVs, we first constructed scattered plots, in which the average oligomeric size per single GUV and protein surface concentration, two different read-outs of dual-(+1)-FCS, are correlated for both the INITIAL (**Figure 21A**) and FINAL states (**Figure 21B**).

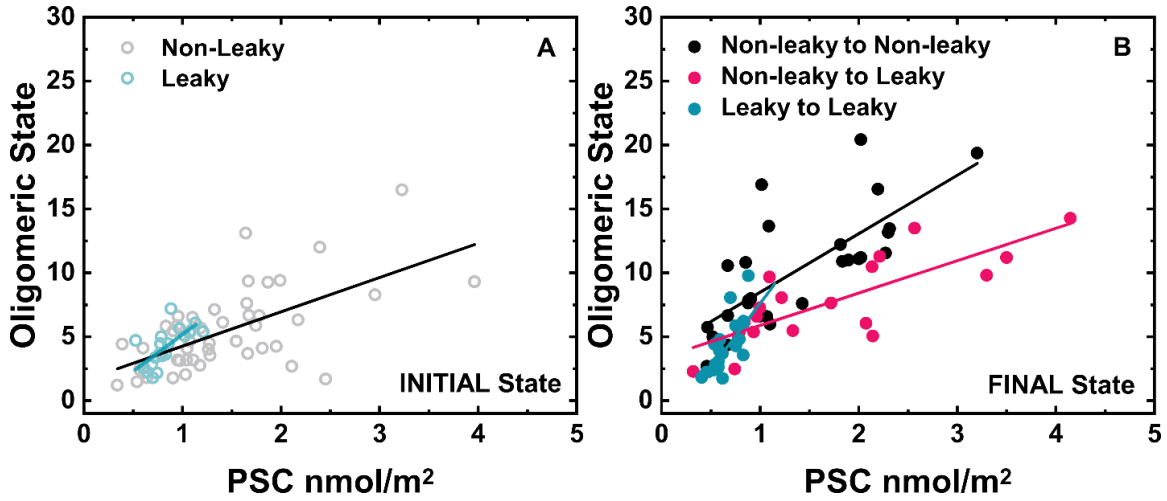

Figure 21: PSC correlation with oligomeric state (an individual GUV's study in a time-resolved manner). (A) This panel shows the INITIAL State of GUVs; grey represents non-leaky, and cyan represents leaky vesicles. (B) This panel shows the FINAL State of vesicles, e.g. black dots represent non-leaky to non-leaky GUVs.

The population of (leaky → leaky) GUVs in the FINAL state contrasts sharply with the remaining two GUV populations of (non-leaky → non-leaky) or (non-leaky → leaky) GUVs in the same state. More specifically, the data points for (leaky → leaky) GUVs are exclusively clustered at the PSC (FGF2-GFP) of less than 1 nmol/m² and ⟨*N*(m.u.)⟩ of less than 10, displaying an average oligomer size ⟨*N*(m.u.)⟩ = 4.21 ± 2.073 and PSC = 0.64 ± 0.139 nmol/m². In contrast, the data points for (non-leaky → non-leaky) and (non-leaky → leaky) GUVs are more widely dispersed, spanning a broad range of PSC ∈ ⟨0;4.1⟩ and ⟨*N*(m.u.)⟩ ∈ ⟨1;20⟩, with a shift toward higher PSC and ⟨*N*(m.u.)⟩. Specifically, for (nonleaky → nonleaky) GUVs, ⟨*N*(m.u.)⟩ = 10.3 ± 4.439 and PSC = 1.39 ± 0.716 nmol/m², and for (nonleaky → leaky) GUVs, ⟨*N*(m.u.)⟩ = 7.64 ± 3.256 and PSC = 1.7 ± 1.23 nmol/m². Additionally, there is an observed increase in oligomer size with rising protein surface concentration, with this dependence appearing more pronounced for (leaky → leaky) GUVs compared to the other two sets.

These findings suggest that the process of FGF2 oligomerization differs between disrupted and intact GUVs. On (leaky → leaky) GUVs, a substantial portion of FGF2 becomes membrane-inserted, facilitating specific oligomerization through cysteine C95 and C77. This proposition gains support from the previously mentioned steep correlation between ⟨*N*(m.u.)⟩

and PSC on (leaky → leaky) GUVs, which is an anticipated outcome of heightened sensitivity to PSC when oligomerization is specifically driven.

In contrast, (non-leaky → non-leaky) vesicles present a clearly distinct scenario regarding protein insertion. Here, non-specific oligomerization of FGF2 leads to the formation of large membrane-associated protein aggregates that do not penetrate the membrane, and their self-assembly is facilitated by higher PSC values. As this population of oligomers lacks the specificity driving protein oligomerization, the resulting dependence of ⟨*N*(m.u.)⟩ on PSC appears less steep and more chaotic, with a less discernible trend (see **Figure 21**).

The remaining subset of (non-leaky → leaky) GUVs, as depicted in **Figure 21**, typically becomes leaky with a lag time of 60−180 min. Although these GUVs also contain the inserted protein in the FINAL state (notably, the membrane of these GUVs is permeabilized in the FINAL state), the presence of the inserted protein is overshadowed by nonspecifically aggregated protein oligomers that formed in excess during the INITIAL state. Consequently, this group of vesicles exhibits properties more similar to (non-leaky → non-leaky) GUVs containing nonfunctional aggregated proteins in excess.

As for the INITIAL state shown in **Figure 21,** the data points representing non-leaky GUVs are widely scattered across a broad range of PSC and oligomer sizes. This wide scattering suggests a variety of oligomerization behaviors, indicative of non-specific protein oligomerization. This implies that a higher concentration of surface-bound protein does not necessarily lead to membrane permeabilization, but rather to protein aggregation. In contrast, the data points representing leaky GUVs are more tightly clustered within a narrower range of PSC and smaller oligomer sizes. The average oligomer size for leaky GUVs is smaller, indicating that smaller oligomers are more effective at causing membrane leaks in the INITIAL state. Overall, the analysis of the INITIAL state highlights the importance of both protein surface concentration and oligomer size in determining the permeabilization behavior of FGF2.

4.4 Linking diffusion coefficient of membrane-associated FGF2 to its oligomerization

Similar to the scatter plot linking the oligomeric state of FGF2 with PCS (**Figure 18**), analogous dependencies can be generated linking the typical output parameter of FCS, the diffusion coefficient of membrane-associated FGF2, with PSC or with *N*(m.u.). Thus, a valuable set of several parameters, *N*(m.u) versus PSC, versus *D* or versus membrane permeability, can be correlated using dual-(+1)-FCS. However, as is evident from **Figure 22**, there is no strong correlation between *D* and PSC or between *N*(m.u.) and *D* in the case of FGF2, with the individual data points being distributed more or less randomly. At the same time, from a physics point of view, it is reasonable to assume that the diffusion coefficient of FGF2 should gradually decrease with increasing oligomer size. The reason for the absence of this logical trend is the fact that the big FGF2 oligomers are not embedded in the membrane but only associated with it, which noticeably accelerates its diffusion. Conversely, the small FGF2 oligomers, which should move faster, are embedded in the membrane, which slows them down noticeably. The result is an unclear correlation between *D* versus *N*(m.u.) and *D* versus PSC.

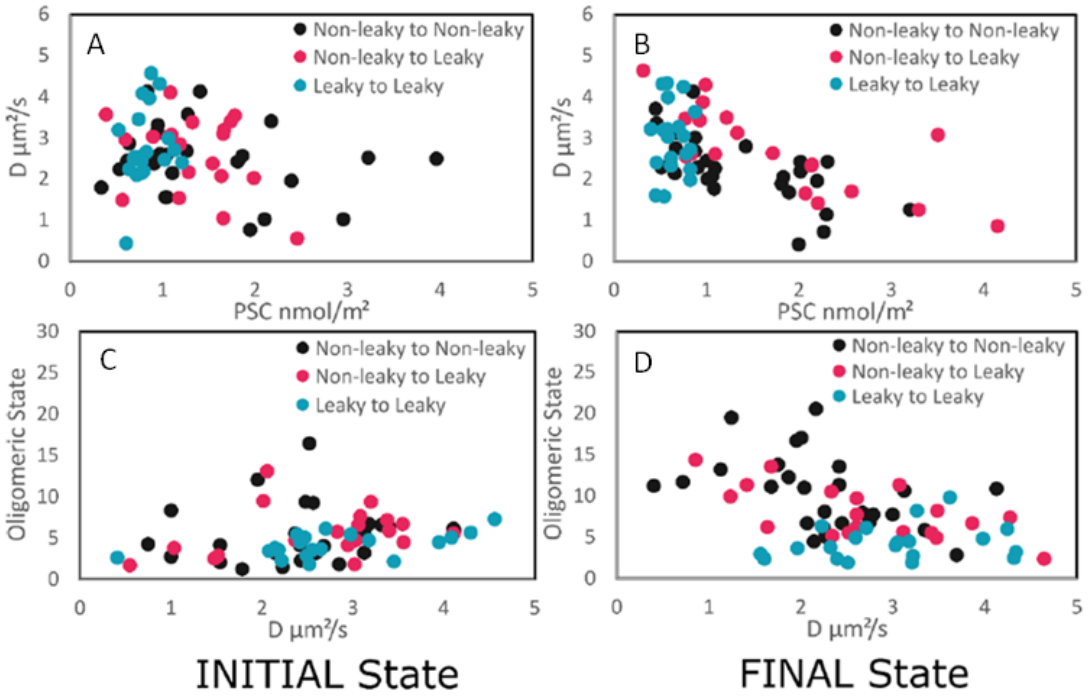

Figure 22: Correlation of the average diffusion coefficient of FGF2 to PSC (upper row), as well as the oligomeric state to the diffusion coefficient of FGF2 (lower row) for all three populations considered throughout the work.

4.5 Understanding the journey of pore formation

In the next step, for the extended set of GUVs (see the section above), we generated histograms of *N*(m.u.) and PSC for each state as a function of the permeability of the detected vesicles. Interestingly, in the initial state, dimers to hexamers emerge as the predominant species on leaky GUVs (**Figure 23(A1, A2**). The similarity observed in the histograms constructed for the INITIAL and FINAL states (compare **Figure 23(1)** with **Figure 23(2)**) led us to conclude that membrane-inserted protein oligomers do not aggregate over time. Secondly, we inferred that the specific oligomerization of FGF2 occurs within a time scale shorter than 60 minutes. This finding aligns with recent single-molecule cell experiments demonstrating the translocation of FGF2 across the plasma membrane in the order of hundreds of milliseconds145.

Is There a Pre-INITIAL State? Considering this disparity between the short translocation time of FGF2 in cells and the 60-minute incubation time employed in the experiment, we decided to minimize the incubation time in our experimental setup. Consequently, we initiated a dual-(+1)-FCS measurement immediately after introducing the protein to the vesicles and continued monitoring the same set of GUVs for a duration of 30 minutes. For simplicity, our focus was solely on vesicles exhibiting leakage in this pre-INITIAL state. We then compared the obtained histograms representing the protein's oligomeric states with the histograms for the INITIAL state (**Figure 23A**). Scrutinising these histograms reveals that the respective distributions remain unchanged over time. Consequently, the measurement we conducted gives unbiased information about the distribution of membrane-inserted FGF2 oligomers on the membrane. Additionally, it underscores that the specific self-assembly of FGF2 oligomers surpasses the resolution capabilities of this approach.

Furthermore, upon closer inspection of **Figure 23A**, however, a small fraction of large oligomers in the FINAL state on (leaky → leaky) GUVs becomes apparent, absent in the INITIAL state. Consequently, it is more precise to characterize the population of functional membrane-inserted FGF2 by considering only the histogram obtained for the INITIAL state.

Importantly, the scenario differs significantly for the populations of (non-leaky → non-leaky) and (non-leaky → leaky) GUVs, where FGF2 aggregates non-specifically. In these cases, large protein clusters present in the FINAL state are largely missing in the INITIAL state.

In the INITIAL state, dimers to hexamers represent the most dominant oligomer species on both leaky and non-leaky GUVs (see **Figure 23**).

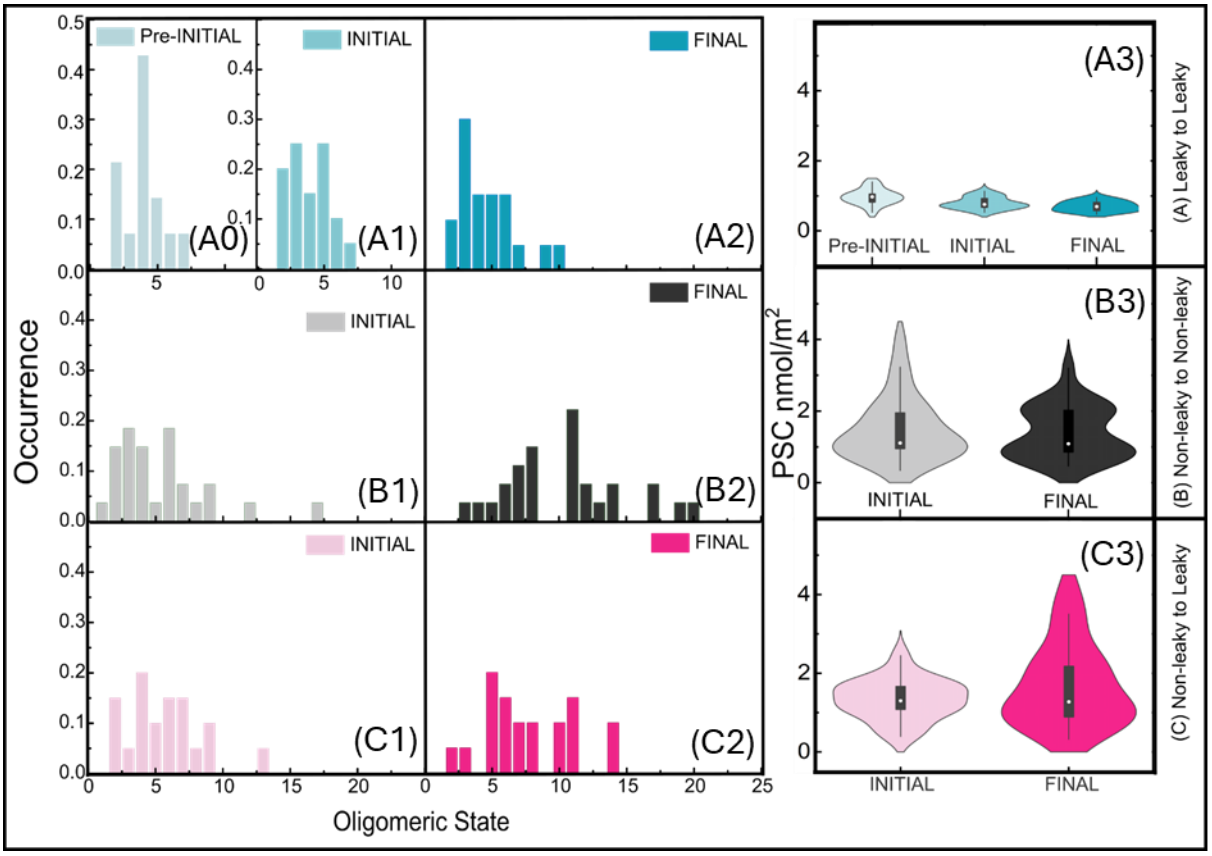

Figure 23: Time-dependent FGF2 oligomer sizes distribution. Top row represents leaky to leaky, middle row represents non-leaky to non-leaky and the lowest row non-leaky to leaky vesicle populations. Violin plots (A3,B3,C3) showing the distribution of PSC for each vesicle population in the Pre-INITIAL, INTITAL and FINAL states are displayed on the right-hand side of the figure.

Overall, our analysis let us conclude that on (non-leaky → non-leaky) and (non-leaky → leaky) GUVs, FGF2 aggregates in a non-specific manner, forming larger oligomers in the FINAL state. Conversely, in the INITIAL state on the leaky GUVs, the dominant oligomeric sizes are in the range of dimers to hexamers, indicating a specific oligomerization process occurring at this stage. The INITIAL state of leaky GUVs, where dimers to hexamers are the dominant species, thus represents the biologically more relevant oligomerization state of FGF2. In contrast, the FINAL state, characterized by non-specific aggregation, is less representative. Consequently, to measure biologically relevant oligomerization numbers of FGF2, it is important to focus on shorter incubation times, as done for the Pre-INITIAL and INITIAL

states before non-specific aggregation occurs, and select from the large ensemble of GUVs only those that are permeabilized.

For a more detailed quantification of the observed changes, we further replotted the data, aiming to highlight the changes in *N*(m.u.) and PSC for all four GUV categories (**Figure 24**). This approach facilitated a further categorization of GUVs into four contiguous quadrants. These quadrants categorize GUVs based on whether there was a simultaneous increase in ΔPSC and Δ*N*(m.u.) (quadrant I), a decrease in ΔPSC and an increase in Δ*N*(m.u.) (quadrant II), a decrease in both ΔPSC and *Δ*N(m.u.) (quadrant III), or an increase in ΔPSC and a decrease in Δ*N*(m.u.) (quadrant IV).

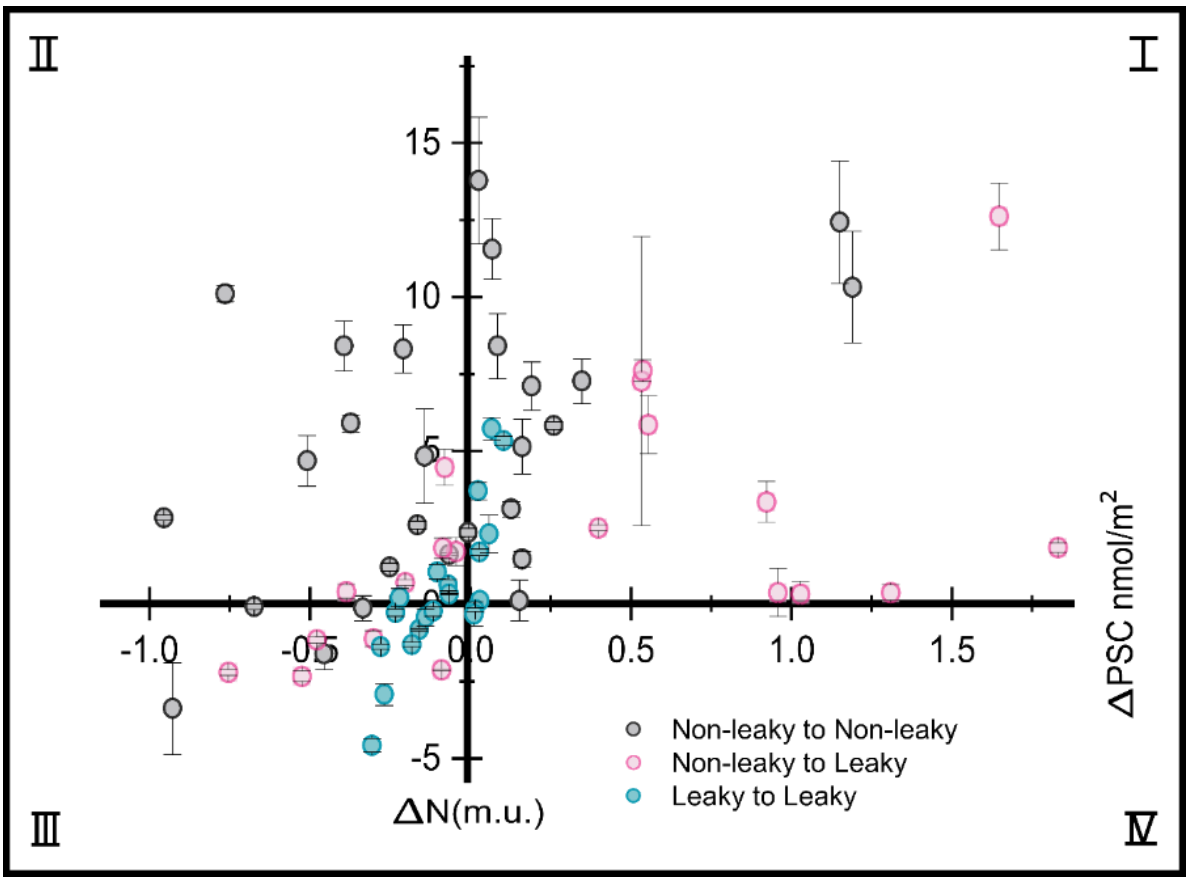

Figure 24: Correlation of $\Delta\langle N(\mathrm{m.u.})\rangle$ and ΔPSC against each other. Each dot represents a GUV.

Even in this graphical representation, the (leaky → leaky) vesicle population exhibits a noticeable distinction from the other two populations. Events are distributed relatively evenly among quadrants I to III, with approximately an equal number of vesicles displaying positive or negative *Δ*N(m.u.) or ΔPSC values (refer to **Table 1**). Additionally, the changes in PSC are relatively small, with a relative change of approximately 10−20%. In contrast, the alterations

in ⟨*N*(m.u.)⟩ reach a maximum of +3 monomeric units in quadrant I and only +0.8 m.u. in quadrant II.

In contrast, within the (non-leaky → non-leaky) vesicles, 85% of all GUVs exhibit an increase in the average number of monomer units (⟨*N*(m.u.)⟩), with the change (Δ*N*(m.u.)) in the first quadrant averaging up to seven monomer units. This suggests a significant oligomerization process occurring non-specifically, even in the absence of membrane leakage. In the (non-leaky → leaky) population, which includes a fraction of specifically oligomerized FGF2, the increase is less pronounced but still noteworthy: 75% of all vesicles display an increase in ⟨*N*(m.u.)⟩, with an average addition of four monomer units in quadrant I.

Table 1. The changes in both the average protein surface concentration and average protein oligomeric states on individual GUVs calculated for quadrants I-IV as well as for all GUV populations under consideration.

quad	[Δ*N*(m.u.), ΔPSC]	nonleaky to nonleaky			nonleaky to leaky			leaky to leaky		
		no. of GUVs	<Δ*N*(m.u.)>	<ΔPSC>	no. of GUVs	<Δ*N*(m.u.)>	<ΔPSC>	no. of GUVs	<Δ*N*(m.u.)>	<ΔPSC>
I	[+,+]	12	7.2 ± 4.34	0.32 ± 0.408	10	4.2 ± 4.04	0.98 ± 0.50	6	3.3 ± 2.16	0.05 ± 0.030
II	[+,-]	11	4.8 ± 3.04	-0.35 ± 0.295	5	1.8 ± 1.61	-0.14 ± 0.13	5	0.8 ± 0.52	-0.11 ± 0.072
III	[-,-]	4	-1.36 ± 1.56	-0.60 ± 0.254	5	-1.8 ± 0.59	-0.42 ± 0.246	7	-1.3 ± 1.57	-0.21 ± 0.071
IV	[-,+]							2	-0.2 ± 0.19	0.01 ± 0.003

Furthermore, the ΔPSC in quadrant I is up to 19 times larger in the (non-leaky → non-leaky) vesicles compared to the (leaky → leaky) vesicles, where non-specific protein aggregation is minimal (refer to **Table 1**). This substantial difference underscores the specificity of FGF2 oligomerization in (leaky → leaky) vesicles, contrasting with more scattered changes observed in (non-leaky →non- leaky) vesicles, where non-specific aggregation is prevalent.

4.6 Comparison of STED microscopy oligomerization data with dual-(+1)-FCS

To highlight the importance of filtering GUVs before constructing the final histogram of oligomer sizes, we revisited our previous data showing the unfiltered histogram of FGF2 oligomer sizes measured by STED microscopy on supported phospholipid bilayers [69].

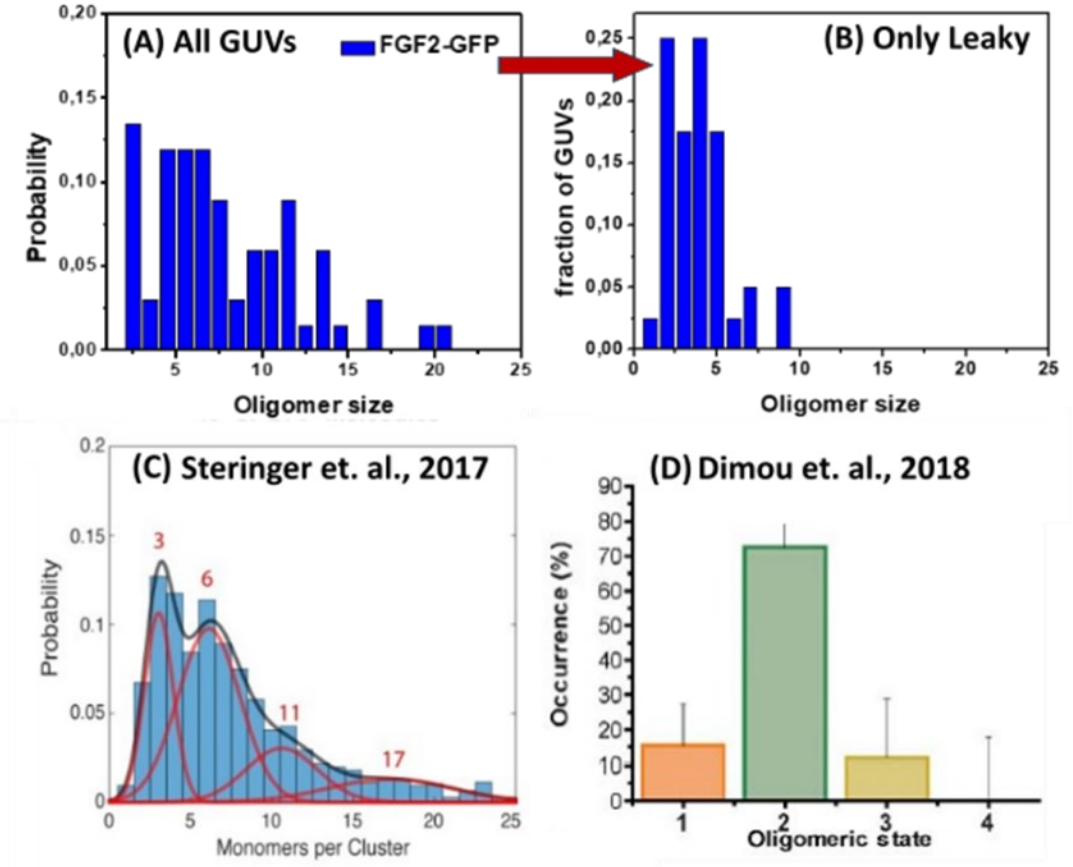

Figure 25: (A) Distribution of oligomeric states of FGF2-GFP without any filtering (i.e., without classifying GUVs as leaky or non-leaky) as determined by dual-(+1)-FCS. (B) Distribution of oligomeric states for FGF2-GFP with a filter applied for leaky GUVs only. (C) The broad distribution of oligomeric states of FGF2-Y81pCMF-Halo-StarRed on supported lipid bilayers from the previous work by *Steringer et al., eLife 2017[69]* determined by STED. (D) FGF2 oligomeric state as determined by *Dimou et al. 2018 [99]* on the plasma membranes of living cells with single molecule localisation microscopy.

When reconstituted in SPBs, FGF2 oligomerizes into multimers with a wide distribution of oligomer sizes (**Figure 25C**). More specifically, STED microscopy identified oligomers ranging from dimers to very large 24-mers within SPBs. Using Gaussian distribution

revealed four distinct components corresponding to oligomers with 3, 6, 11, and 17 monomers per cluster, as identified by *Steringer et al.[69]* . Interestingly, when dual-(+1)-FCS was used without applying any filtering criteria, a similarly broad distribution of oligomer sizes was observed (**Figure 25A**). Without filtering, all vesicles are included in the analysis, even those with non-specifically aggregated proteins. This, however, indicates that not every oligomer detected with STED microscopy is capable of forming a membrane pore.

Conversely, if only GUVs containing the majority of the protein functionally embedded in the membrane (represented by leaky GUVs in the INITIAL state) are selected, the distribution of FGF2 oligomeric states becomes significantly narrower and more closely matches the oligomeric states detected in the plasma membranes of living cells (**Figure 25BD**). Specifically, in this case, only monomers, dimers, and a small fraction of trimers were observed105. However, this in vivo approach may underestimate the real content of larger aggregates105. Therefore, a clear challenge for the future is to find a better intersection between in vivo and in vitro experiments and to determine which FGF2 oligomers are present in the membrane during translocation. Our results thus demonstrate the necessity of testing the functionality of individually detected protein oligomers reconstituted in biological model membrane systems. Not all membrane-associated oligomers may be functional or have the same characteristics.

5. Conclusions

In this dissertation, a novel single-vesicle, single-molecule fluorescence assay was developed to monitor pore formation by tracking the clustering of individual protein molecules. The effectiveness of this approach was demonstrated by studying the translocation of Fibroblast Growth Factor 2 (FGF2) across vesicle membranes, which is accompanied by FGF2 oligomerization and the formation of transmembrane pores.

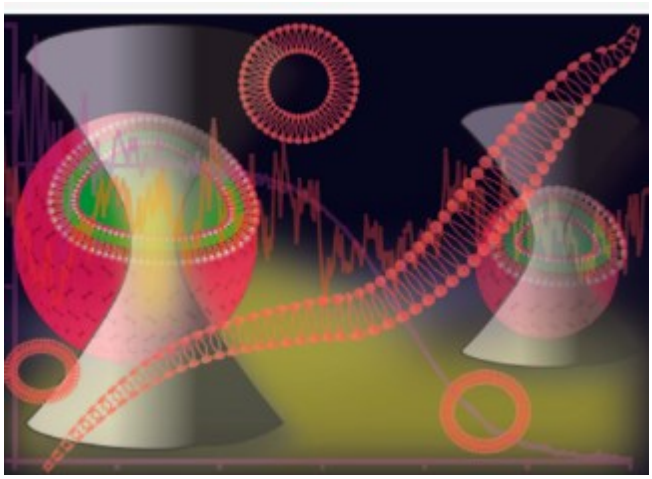

5.1 Part I: Development of a functional dual-(+1)-FCS assay to correlate protein oligomerization states with membrane pore formation.

Specifically, in the first part of the dissertation, the dual-(+1)-FCS single GUV assay was developed as an advanced single-molecule fluorescence method. This assay is designed to study protein-membrane interactions that lead to protein oligomerization and the subsequent formation of membrane pores. By analyzing fluctuations in fluorescence intensity and determining the brightness of individual fluorescent species as they diffuse within the GUV membrane, this method provides information on protein surface concentration, diffusion coefficient, and protein oligomeric state, specifically in leaky versus non-leaky vesicles (i.e., membrane-permeabilized versus intact vesicles).

Increased membrane permeability indicates pore formation, while an intact membrane suggests no pore formation. Importantly, this method uses free-standing membranes, which, unlike supported lipid bilayers, do not affect protein mobility and are better suited for monitoring membrane pore formation. Overall, the assay directly correlates the degree of

protein oligomerization within the membrane to pore formation, offering valuable insights into the mechanisms of membrane permeabilization by proteins.

5.2 Part II: Determining the functional oligomeric state of membrane-associated FGF2 oligomers forming membrane pores on giant lipid vesicles.

In the second part of the dissertation, the dual-(+1)-FCS single GUV assay was applied to study the translocation of FGF2 across giant lipid vesicle membranes. This process is accompanied by in-membrane protein oligomerization and the formation of membrane pores.

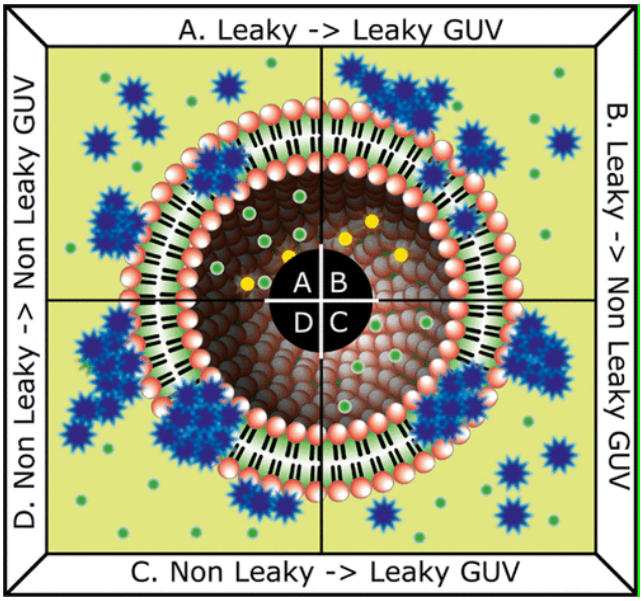

We demonstrated that the wide range of in-membrane oligomer states of FGF2, typically observed on supported lipid bilayers, arises from a mixture of complexes with different properties. Specifically, we identified two distinct populations of FGF2: one consisting mainly of membrane-inserted dimers to hexamers that cause membrane permeabilization and another comprising non-specifically aggregated proteins associated with the membrane, which do not necessarily reflect functional oligomerization processes.

By using dual-(+1)-FCS in a time-resolved mode, we were able to track the oligomerization of membrane-associated FGF2 over time. This tracking revealed that FGF2 aggregates on GUVs over time without causing leakage, significantly broadening the final distribution of oligomer sizes. By linking oligomer size to a functional readout involving

membrane permeability, we successfully filtered out the unwanted contribution of non-specifically aggregated proteins. This approach allowed us to refine the oligomer size distribution recorded previously by STED microscopy on supported phospholipid bilayers.

In conclusion, our study illustrates the complex nature of protein oligomerization and emphasizes the need for careful analysis to differentiate between specific and nonspecific aggregation processes. It highlights that merely determining the oligomerization states of proteins can yield biased results, as the observed distribution of oligomer sizes may be multimodal due to the presence of both specific and nonspecific protein aggregates.

Supplementary Information

Material and Methods

Giant Unilamellar Vesicles: All lipids used for GUV preparation were supplied by Avanti Polar Lipids. GUVs with a PM like lipid composition were prepared using the following lipids: 33 mol% phosphatidylcholine (DOPC), 10 mol% phosphatidylethanolamine (DOPE), 5 mol% phosphatidylserine (DOPS), 5 mol% phosphatidylinositol (DOPI), 15 mol% sphingomyelin (SM), 30 mol% cholesterol (Chol), 1 mol% Biotinyl-PE and 0.05 mol% dioleolyl-PE labelled in the headgroup by Atto-633 (DOPE-Atto-633, ATTO-TEC). GUVs were generated based on electro-swelling using platinum electrodes[141, 142] . GUVs were supplemented with either 2 mol% phosphatidylinositol-4,5-bisphosphate (PIP2) or a DGS-NTA lipid (Avanti Polar Lipids). The dried lipid film was hydrated with a 300 mM sucrose solution (300 mOsmol/kg). Electro-swelling was conducted at 45˚C (10 Hz, 1.5 V for 50 min, 2 Hz, 1.5 V for 25 min). GUVs were gently washed with HEPES buffer (25 mM HEPES pH 7.4, 150 mM NaCl, 310 mOsmol/kg) and collected via centrifugation (1200x g; 25˚C; 5 min). The loose GUV pellet was carefully resuspended in a small volume of HEPES buffer and diluted again in 11.5 ml buffer, followed by centrifugation (1200x g; 25˚C; 5 min). The supernatant was removed while the loose GUV pellet was carefully resuspended. Imaging chambers (IBIDI uncoated) were incubated sequentially with 0.1 mg/ml Biotin-BSA (Sigma) and 0.1 mg/ml Neutravidin (Thermo Fisher Scientific) dissolved in MilliQ water.

Protein Expression and Purification

FGF2 used in part I: His-FGF2-Y81pCMF-GFP, His-FGF2-Y81pCMF-C77/95A-GFP and His-FGF2-Y81pCMF-C77/95A were expressed in E. coli strains W3110Z1 or BL21 Star (DE3), respectively. For incorporation of the unnatural amino acid p-carboxylmethylphenylalanine (pCMF; custom synthesis by ENAMINE Ltd., Kiev, Ukraine), codon 81 (tyrosine) was replaced by an amber stop codon. Transformation of a strain carrying the pEVOL-pCMF plasmid resulted in expression of recombinant His-FGF2-Y81pCMF. All proteins were purified in three steps via Ni-NTA affinity chromatography, heparin chromatography and size exclusion chromatography using a Superdex 75 column [138].

FGF2 used in part II: His-tagged variants of FGF2-GFP (pET15b) were expressed in Escherichia coli strain BL21 Star (DE3). All proteins were purified in three steps via Ni-NTA affinity chromatography, heparin chromatography, and size-exclusion chromatography using a superdex 75 column.(protein purified done by Walter Nickel lab in Heidelberg, Germany) [137].

Bibliography

[1] De Weer P. A Century of Thinking About Cell Membranes. *Annu Rev Physiol* 2000; 62: 919–926.

[2] Lombard J. Once upon a time the cell membranes: 175 years of cell boundary research. *Biol Direct* 2014; 9: 32.

[3] Nicolson GL. The Fluid—Mosaic Model of Membrane Structure: Still relevant to understanding the structure, function and dynamics of biological membranes after more than 40 years. *Biochimica et Biophysica Acta (BBA) - Biomembranes* 2014; 1838: 1451–1466.

[4] Pomorski T, Hrafnsdóttir S, Devaux PF, et al. Lipid distribution and transport across cellular membranes. *Semin Cell Dev Biol* 2001; 12: 139–148.

[5] Watts A. Membrane structure and dynamics. *Curr Opin Cell Biol* 1989; 1: 691–700.

[6] Bradbury NA, Bridges RJ. Role of membrane trafficking in plasma membrane solute transport. *American Journal of Physiology-Cell Physiology* 1994; 267: C1–C24.

[7] Stillwell W. Chapter 19 - Membrane Transport. In: Stillwell W (ed) *An Introduction to Biological Membranes* (Second Edition). Elsevier, 2016, pp. 423–451

[8] Schwarz G, Robert CH. Kinetics of pore-mediated release of marker molecules from liposomes or cells. *Biophys Chem* 1992; 42: 291–296.

[9] Gilbert RJC. Protein-lipid interactions and non-lamellar lipidic structures in membrane pore formation and membrane fusion. *Biochimica et Biophysica Acta (BBA) - Biomembranes* 2016; 1858: 487–499.

[10] Mesa-Galloso H, Pedrera L, Ros U. Pore-forming proteins: From defense factors to endogenous executors of cell death. *Chem Phys Lipids* 2021; 234: 105026.

[11] Ros U, García-Sáez AJ. More Than a Pore: The Interplay of Pore-Forming Proteins and Lipid Membranes. *J Membr Biol* 2015; 248: 545–561.

[12] Evans JC, Tweten RK. Chapter Two - How protein engineering has revealed the molecular mechanisms of pore-forming toxins. In: Heuck AP (ed) *Methods in Enzymology*. Academic Press, pp. 47–70.

[13] Gilbert RJC, Serra MD, Froelich CJ, et al. Membrane pore formation at protein-lipid interfaces. *Trends in Biochemical Sciences* 2014; 39: 510–516.

[14] Peraro MD, van der Goot FG. Pore-forming toxins: ancient, but never really out of fashion. *Nat Rev Microbiol* 2016; 14: 77–92.

[15] Voskoboinik I, Whisstock JC, Trapani JA. Perforin and granzymes: function, dysfunction and human pathology. *Nat Rev Immunol* 2015; 15: 388–400.

[16] Prinz D, Klein K, List J, et al. Loss of NKG2D in murine NK cells leads to increased perforin production upon long-term stimulation with IL-2. *Eur J Immunol* 2020; 50: 880–890.

[17] Gonzalez MR, Bischofberger M, Pernot L, et al. Bacterial pore-forming toxins: The (w)hole story? *Cellular and Molecular Life Sciences* 2008; 65: 493–507.

[18] Flores-Romero H, Ros U, Garcia-Saez AJ. Pore formation in regulated cell death. *EMBO J* 2020; 39: e105753.

[19] Los, F. C. O., Randis, T. M., Aroian et al. Role of Pore-Forming Toxins in Bacterial Infectious Diseases. *Microbiology and Molecular Biology Reviews* 2013; 77: 173–207.

[20] Črnigoj Kristan K, Viero G, Dalla Serra M, et al. Molecular mechanism of pore formation by actinoporins. *Toxicon* 2009; 54: 1125–1134.

[21] Rosado CJ, Kondos S, Bull TE, et al. The MACPF/CDC family of pore-forming toxins. *Cell Microbiol* 2008; 10: 1765–1774.

[22] Kovacs SB, Miao EA. Gasdermins: Effectors of Pyroptosis. *Trends Cell Biol* 2017; 27: 673–684.

[23] Espiritu RA, Pedrera L, Ros U. Chapter Seven - Tuning the way to die: implications of membrane perturbations in necroptosis. In: Iglič A, Rappolt M, García-Sáez AJ (eds) *Advances in Biomembranes and Lipid Self-Assembly*. Academic Press, pp. 201–247.

[24] Flores-Romero H, García-Sáez AJ. Lipids glue BAK dimers together. *Nat Struct Mol Biol* 2020; 27: 1003–1004.

[25] Liu X, Zhang Z, Ruan J, et al. Inflammasome-activated gasdermin D causes pyroptosis by forming membrane pores. *Nature* 2016; 535: 153–158.

[26] Cosentino K, García-Sáez AJ. Bax and Bak Pores: Are We Closing the Circle? *Trends in Cell Biology* 2017; 27: 266–275.

[27] Flores-Romero H, García-Sáez AJ. The Incomplete Puzzle of the BCL2 Proteins. *Cells*; 8. Epub ahead of print 1 October 2019.

[28] Rojko N, Anderluh G. How Lipid Membranes Affect Pore Forming Toxin Activity. *Acc Chem Res* 2015; 48: 3073–3079.

[29] Cosentino K, Ros U, García-Sáez AJ. Assembling the puzzle: Oligomerization of α-pore forming proteins in membranes. *Biochim Biophys Acta Biomembr* 2016; 1858: 457–466.

[30] Iacovache I, Bischofberger M, van der Goot FG. Structure and assembly of pore-forming proteins. *Curr Opin Struct Biol* 2010; 20: 241–6.

[31] Omersa N, Podobnik M, Anderluh G. Inhibition of pore-forming proteins. *Toxins*; 11. Epub ahead of print 19 September 2019.

[32] Chan YHM, Boxer SG. Model membrane systems and their applications. *Current Opinion in Chemical Biology* 2007; 11: 581–587.

[33] Siontorou CG, Nikoleli GP, Nikolelis DP, et al. Artificial lipid membranes: Past, present, and future. *Membranes*; 7. Epub ahead of print 1 September 2017.

[34] Céspedes PF, Beckers D, Dustin ML, et al. Model membrane systems to reconstitute immune cell signaling. *FEBS J* 2021; 288: 1070–1090.

[35] Ong SGM, Chitneni M, Lee KS, et al. Evaluation of extrusion technique for nanosizing liposomes. *Pharmaceutics*; 8. Epub ahead of print 21 December 2016.

[36] Walde P, Cosentino K, Engel H, et al. Giant Vesicles: Preparations and Applications. *ChemBioChem* 2010; 11: 848–865.

[37] Dimova R, Riske KA. Electrodeformation, Electroporation, and Electrofusion of Giant Unilamellar Vesicles. In: Miklavčič D (ed) *Handbook of Electroporation*. Cham: Springer International Publishing, pp. 235–252.

[38] Sezgin E, Schwille P. Model membrane platforms to study protein-membrane interactions. *Mol Membr Biol* 2012; 29: 144–154.

[39] Tamm LK, McConnell HM. Supported phospholipid bilayers. *Biophys J* 1985; 47: 105–113.

[40] Reviakine I, Brisson A. Formation of supported phospholipid bilayers from unilamellar vesicles investigated by atomic force microscopy. *Langmuir* 2000; 16: 1806–1815.

[41] Ulmefors H, Nissa J, Pace H, et al. Formation of Supported Lipid Bilayers Derived from Vesicles of Various Compositional Complexity on Conducting Polymer/Silica Substrates. *Langmuir* 2021; 37: 5494–5505.

[42] Roder F, Waichman S, Paterok D, et al. Reconstitution of membrane proteins into polymer-supported membranes for probing diffusion and interactions by single molecule techniques. *Anal Chem* 2011; 83: 6792–6799.

[43] Tanaka M, Sackmann E. Polymer-supported membranes as models of the cell surface. *Nature* 2005; 437: 656–663.

[44] McCabe IP, Forstner MB. Polymer Supported Lipid Bilayers. *Open J Biophys* 2013; 03: 59–69.

[45] Roder F, Birkholz O, Beutel O, et al. Spatial organization of lipid phases in micropatterned polymer-supported membranes. *J Am Chem Soc* 2013; 135: 1189–1192.

[46] Su H, Liu HY, Pappa AM, et al. Facile Generation of Biomimetic-Supported Lipid Bilayers on Conducting Polymer Surfaces for Membrane Biosensing. *ACS Appl Mater Interfaces* 2019; 11: 43799–43810.

[47] Denisov IG, Sligar SG. Nanodiscs for structural and functional studies of membrane proteins. *Nature Structural and Molecular Biology* 2016; 23: 481–486.

[48] Bayburt TH, Sligar SG. Membrane protein assembly into Nanodiscs. *FEBS Letters* 2010; 584: 1721–1727.

[49] Guha S, Ghimire J, Wu E, et al. Mechanistic Landscape of Membrane-Permeabilizing Peptides. *Chem Rev* 2019; 119: 6040–6085.

[50] Marchioretto M, Podobnik M, Dalla Serra M, et al. What planar lipid membranes tell us about the pore-forming activity of cholesterol-dependent cytolysins. *Biophys Chem* 2013; 182: 64–70.

[51] Ulbrich MH, Isacoff EY. Subunit counting in membrane-bound proteins. *Nat Methods* 2007; 4: 319–321.

[52] Ha T, Enderle T, Ogletree DF, et al. Probing the interaction between two single molecules: fluorescence resonance energy transfer between a single donor and a single acceptor. *Proceedings of the National Academy of Sciences* 1996; 93: 6264–6268.

[53] Ries J, Petrášek Z, García-Sáez AJ, et al. A comprehensive framework for fluorescence cross-correlation spectroscopy. *New J Phys* 2010; 12: 113009.

[54] Schwille P, Meyer-Almes FJ, Rigler R. Dual-color fluorescence cross-correlation spectroscopy for multicomponent diffusional analysis in solution. *Biophys J* 1997; 72: 1878–1886.

[55] Huang B, Bates M, Zhuang X. Super-resolution fluorescence microscopy. *Annual Review of Biochemistry* 2009; 78: 993–1016.

[56] Loura LMS, Prieto M. FRET in membrane biophysics: An overview. *Front Physiol*; 2 NOV. Epub ahead of print 2011.

[57] Garg P, Nemec KN, Khaled AR, et al. Transmembrane pore formation by the carboxyl terminus of Bax protein. *Biochimica et Biophysica Acta (BBA) - Biomembranes* 2013; 1828: 732–742.

[58] Lidman M, Pokorná Š, Dingeldein APG, et al. The oxidized phospholipid PazePC promotes permeabilization of mitochondrial membranes by Bax. *Biochimica et Biophysica Acta (BBA) - Biomembranes* 2016; 1858: 1288–1297.

[59] Apellániz B, Nieva JL, Schwille P, et al. All-or-None versus Graded: Single-Vesicle Analysis Reveals Lipid Composition Effects on Membrane Permeabilization. *Biophys J* 2010; 99: 3619–3628.

[60] Ladokhin AS, Wimley WC, White SH. Leakage of membrane vesicle contents: determination of mechanism using fluorescence requenching. *Biophys J* 1995; 69: 1964–1971.

[61] Peters K, Richards FM. Chemical Cross-Linking: Reagents and Problems in Studies of Membrane Structure. *Annu Rev Biochem* 1977; 46: 523–551.

[62] Kluger R, Alagic A. Chemical cross-linking and protein–protein interactions—a review with illustrative protocols. *Bioorg Chem* 2004; 32: 451–472.

[63] Hastrup H, Karlin A, Javitch JA. Symmetrical dimer of the human dopamine transporter revealed by cross-linking Cys-306 at the extracellular end of the sixth transmembrane segment. *Proc Natl Acad Sci U S A* 2001; 98: 10055–10060.

[64] Joseph MD, Bort ET, Grose RP, et al. Quantitative super-resolution imaging for the analysis of GPCR oligomerization. *Biomolecules*; 11. Epub ahead of print 1 October 2021.

[65] Salvador-Gallego R, Mund M, Cosentino K, et al. Bax assembly into rings and arcs in apoptotic mitochondria is linked to membrane pores. *EMBO J* 2016; 35: 389-401–401.

[66] Hell SW, Wichmann J. Breaking the diffraction resolution limit by stimulated emission: stimulated-emission-depletion fluorescence microscopy. *Opt Lett* 1994; 19: 780–782.

[67] Klar TA, Hell SW. Subdiffraction resolution in far-field fluorescence microscopy. *Opt Lett* 1999; 24: 954–956.

[68] Donnert G, Keller J, Medda R, et al. Macromolecular-scale resolution in biological fluorescence microscopy. *Proceedings of the National Academy of Sciences* 2006; 103: 11440–11445.

[69] Steringer JP, Lange S, Čujová S, et al. Key steps in unconventional secretion of fibroblast growth factor 2 reconstituted with purified components. *Elife* 2017; 6: e28985.

[70] Nolan R, Iliopoulou M, Alvarez L, et al. Detecting protein aggregation and interaction in live cells: A guide to number and brightness. *Methods* 2018; 140–141: 172–177.

[71] Qian H, Elson EL. On the analysis of high order moments of fluorescence fluctuations. *Biophys J* 1990; 57: 375–380.

[72] Digman MA, Dalal R, Horwitz AF, et al. Mapping the Number of Molecules and Brightness in the Laser Scanning Microscope. *Biophys J* 2008; 94: 2320–2332.

[73] Fukushima R, Yamamoto J, Kinjo M. Empirical Bayes method using surrounding pixel information for number and brightness analysis. *Biophys J* 2021; 120: 2156–2171.

[74] Fukushima R, Yamamoto J, Kinjo M. Number and Brightness Analysis: Visualization of Protein Oligomeric State in Living Cells. In: Kim JK, Kim JK, Pack C-G (eds) *Advanced Imaging and Bio Techniques for Convergence Science*. Singapore: Springer Singapore, pp. 31–58.

[75] Fukushima R, Yamamoto J, Ishikawa H, et al. Two-detector number and brightness analysis reveals spatio-temporal oligomerization of proteins in living cells. *Methods* 2018; 140–141: 161–171.

[76] Ulbrich MH, Isacoff EY. Subunit counting in membrane-bound proteins. *Nat Methods* 2007; 4: 319–321.

[77] Ulbrich MH. Counting Molecules: Toward Quantitative Imaging. In: Tinnefeld P, Eggeling C, Hell SW (eds) *Far-Field Optical Nanoscopy*. Berlin, Heidelberg: Springer Berlin Heidelberg, pp. 263–291.

[78] Hell SW. Microscopy and its focal switch. *Nat Methods* 2009; 6: 24–32.

[79] Betzig E, Patterson GH, Sougrat R, et al. Imaging Intracellular Fluorescent Proteins at Nanometer Resolution. *Science (1979)* 2006; 313: 1642–1645.

[80] Elson EL, Magde D. Fluorescence correlation spectroscopy. I. Conceptual basis and theory. *Biopolymers* 1974; 13: 1–27.

[81] Humpolíčková J, Gielen E, Benda A, et al. Probing Diffusion Laws within Cellular Membranes by Z-Scan Fluorescence Correlation Spectroscopy. *Biophys J* 2006; 91: L23–L25.

[82] Sýkora J, Slavíček P, Jungwirth P, et al. Time-Dependent Stokes Shifts of Fluorescent Dyes in the Hydrophobic Backbone Region of a Phospholipid Bilayer: Combination

of Fluorescence Spectroscopy and Ab Initio Calculations. *J Phys Chem B* 2007; 111: 5869–5877.

[83] Tinnefeld P, Hofkens J, Herten D-P, et al. Higher-Excited-State Photophysical Pathways in Multichromophoric Systems Revealed by Single-Molecule Fluorescence Spectroscopy. *ChemPhysChem* 2004; 5: 1786–1790.

[84] Kask P, Piksarv P, Mets Ü. Fluorescence correlation spectroscopy in the nanosecond time range: Photon antibunching in dye fluorescence. *European Biophysics Journal* 1985; 12: 163–166.

[85] Maurel D, Comps-Agrar L, Brock C, et al. Cell-surface protein-protein interaction analysis with time-resolved FRET and snap-tag technologies: application to GPCR oligomerization. *Nat Methods* 2008; 5: 561–567.

[86] Hoppe A, Christensen K, Swanson JA. Fluorescence Resonance Energy Transfer-Based Stoichiometry in Living Cells. *Biophys J* 2002; 83: 3652–3664.

[87] Škerle J, Humpolíčková J, Johnson N, et al. Membrane Protein Dimerization in Cell-Derived Lipid Membranes Measured by FRET with MC Simulations. *Biophys J* 2020; 118: 1861–1875.

[88] Armelin HA. Pituitary extracts and steroid hormones in the control of 3T3 cell growth (mouse fibroblasts/growth factor). *Proc Natl Acad Sci U S A* 1973; 70: 2702–2706.

[89] Katoh M, Katoh M. FGF signaling network in the gastrointestinal tract (Review). *Int J Oncol* 2006; 29: 163–168.

[90] Ornitz DM, Itoh N. Protein family review: Fibroblast growth factors. *Genome Biol* 2001; 2: reviews3005.1-3005.12.

[91] Sparn C, Dimou E, Meyer A, et al. Glypican-1 drives unconventional secretion of Fibroblast Growth Factor 2. *Elife* 2022; 11: 1–25.

[92] Sparn C, Meyer A, Saleppico R, et al. Unconventional secretion mediated by direct protein self-translocation across the plasma membranes of mammalian cells. *Trends in Biochemical Sciences* 2022; 47: 699–709.

[93] Javerzat S, Auguste P, Bikfalvi A. The role of fibroblast growth factors in vascular development. *Trends in Molecular Medicine* 2002; 8: 483–489.

[94] Zhang J, Cousens LS, Barr PJ, et al. Three-dimensional structure of human basic fibroblast growth factor, a structural homolog of interleukin 1β. *Proc Natl Acad Sci U S A* 1991; 88: 3446–3450.

[95] Wang YJ, Shahrokh Z, Vemuri S, et al. Characterization, stability, and formulations of basic fibroblast growth factor. *Pharmaceutical biotechnology* 1996; 9: 141–180.

[96] VEMURI S, BEYLIN I, SLUZKY V, et al. The Stability of bFGF Against Thermal Denaturation. *Journal of Pharmacy and Pharmacology* 1994; 46: 481–486.

[97] Furue MK, Na J, Jackson JP, et al. Heparin promotes the growth of human embryonic stem cells in a defined serum-free medium. *Proc Natl Acad Sci U S A* 2008; 105: 13409–13414.

[98] Akl MR, Nagpal P, Ayoub NM, et al. Molecular and clinical significance of fibroblast growth factor 2 (FGF2/bFGF) in malignancies of solid and hematological cancers for personalized therapies. *Oncotarget* 2016; 7: 44735–44762.

[99] Dimou E, Nickel W. Unconventional mechanisms of eukaryotic protein secretion. *Current Biology* 2018; 28: R406–R410.

[100] Pallotta MT, Nickel W. FGF2 and IL-1β - Explorers of unconventional secretory pathways at a glance. *J Cell Sci*; 133. Epub ahead of print 1 November 2020.

[101] Malhotra V. Unconventional protein secretion: An evolving mechanism. *EMBO Journal* 2013; 32: 1660–1664.

[102] Rabouille C. Pathways of Unconventional Protein Secretion. *Trends in Cell Biology* 2017; 27: 230–240.

[103] Muesch A, Hartmann E, Rohde K, et al. A novel pathway for secretory proteins? *Trends Biochem Sci* 1990; 15: 86–88.

[104] Nickel W. The mystery of nonclassical protein secretion: A current view on cargo proteins and potential export routes. *European Journal of Biochemistry* 2003; 270: 2109–2119.

[105] Steringer JP, Nickel W. A direct gateway into the extracellular space: Unconventional secretion of FGF2 through self-sustained plasma membrane pores. *Seminars in Cell and Developmental Biology* 2018; 83: 3–7.

[106] Zacherl S, La Venuta G, Müller HM, et al. A Direct Role for ATP1A1 in Unconventional Secretion of Fibroblast Growth Factor 2. *Journal of Biological Chemistry* 2015; 290: 3654–3665.

[107] Legrand C, Saleppico R, Sticht J, et al. The Na,K-ATPase acts upstream of phosphoinositide PI(4,5)P2 facilitating unconventional secretion of Fibroblast Growth Factor 2. *Commun Biol*; 3. Epub ahead of print 1 December 2020.

[108] Temmerman K, Nickel W. A novel flow cytometric assay to quantify interactions between proteins and membrane lipids. *J Lipid Res* 2009; 50: 1245–1254.

[109] Temmerman K, Ebert AD, Müller HM, et al. A direct role for phosphatidylinositol-4,5-bisphosphate in unconventional secretion of fibroblast growth factor 2. *Traffic* 2008; 9: 1204–1217.

[110] Nickel W. The unconventional secretory machinery of fibroblast growth factor 2. *Traffic* 2011; 12: 799–805.

[111] Ebert AD, Laußmann M, Wegehingel S, et al. Tec-Kinase-Mediated Phosphorylation of Fibroblast Growth Factor 2 is Essential for Unconventional Secretion. *Traffic* 2010; 11: 813–826.

[112] Steringer JP, Bleicken S, Andreas H, et al. Phosphatidylinositol 4,5-bisphosphate (PI(4,5)P 2)-dependent oligomerization of fibroblast growth factor 2 (FGF2) triggers the formation of a lipidic membrane pore implicated in unconventional secretion. *Journal of Biological Chemistry* 2012; 287: 27659–27669.

[113] La Venuta G, Wegehingel S, Sehr P, et al. Small molecule inhibitors targeting tec kinase block unconventional secretion of fibroblast growth factor 2. *Journal of Biological Chemistry* 2016; 291: 17787–17803.

[114] Müller HM, Steringer JP, Wegehingel S, et al. Formation of disulfide bridges drives oligomerization, membrane pore formation, and translocation of fibroblast growth factor 2 to cell surfaces. *Journal of Biological Chemistry* 2015; 290: 8925–8937.

[115] Nickel W. Unconventional secretion: An extracellular trap for export of fibroblast growth factor 2. *J Cell Sci* 2007; 120: 2295–2299.

[116] Zehe C, Engling A, Wegehingel S, et al. Cell-surface heparan sulfate proteoglycans are essential components of the unconventional export machinery of FGF-2. *Proc Natl Acad Sci U S A* 2006; 103: 15479–15484.

[117] Nickel W, Seedorf M. Unconventional mechanisms of protein transport to the cell surface of eukaryotic cells. *Annual Review of Cell and Developmental Biology* 2008; 24: 287–308.

[118] Nickel W, Rabouille C. Mechanisms of regulated unconventional protein secretion. *Nat Rev Mol Cell Biol* 2009; 10: 148–155.

[119] Raman R, Venkataraman G, Ernst S, et al. Structural specificity of heparin binding in the fibroblast growth factor family of proteins. *Proc Natl Acad Sci U S A* 2003; 100: 2357–2362.

[120] Nugent MA, Iozzo R V. Fibroblast growth factor-2. *International Journal of Biochemistry and Cell Biology* 2000; 32: 115–120.

[121] Belov AA, Mohammadi M. Molecular mechanisms of fibroblast growth factor signaling in physiology and pathology. *Cold Spring Harb Perspect Biol*; 5. Epub ahead of print June 2013.

[122] Ribatti D, Vacca A, Rusnati M, et al. The discovery of basic fibroblast growth factor/fibroblast growth factor-2 and its role in haematological malignancies. *Cytokine and Growth Factor Reviews* 2007; 18: 327–334.

[123] Presta M, Dell'Era P, Mitola S, et al. Fibroblast growth factor/fibroblast growth factor receptor system in angiogenesis. *Cytokine Growth Factor Rev* 2005; 16: 159–178.

[124] Torrado LC, Temmerman K, Müller HM, et al. An intrinsic quality-control mechanism ensures unconventional secretion of fibroblast growth factor 2 in a folded conformation. *J Cell Sci* 2009; 122: 3322–3329.

[125] Backhaus R, Zehe C, Wegehingel S, et al. Unconventional protein secretion: Membrane translocation of FGF-2 does not require protein unfolding. *J Cell Sci* 2004; 117: 1727–1736.

[126] Merezhko M, Brunello CA, Yan X, et al. Secretion of Tau via an Unconventional Non-vesicular Mechanism. *Cell Rep* 2018; 25: 2027-2035.e4.

[127] Katsinelos T, Zeitler M, Dimou E, et al. Unconventional Secretion Mediates the Trans-cellular Spreading of Tau. *Cell Rep* 2018; 23: 2039–2055.

[128] Debaisieux S, Rayne F, Yezid H, et al. The Ins and Outs of HIV-1 Tat. *Traffic* 2012; 13: 355–363.

[129] Zeitler M, Steringer JP, Möller HM, et al. HIV-Tat protein forms phosphoinositide-dependent membrane pores implicated in unconventional protein secretion. *Journal of Biological Chemistry* 2015; 290: 21976–21984.

[130] Agostini S, Ali H, Vardabasso C, et al. Inhibition of Non Canonical HIV-1 Tat Secretion Through the Cellular Na+,K+-ATPase Blocks HIV-1 Infection. *EBioMedicine* 2017; 21: 170–181.

[131] Rayne F, Debaisieux S, Yezid H, et al. Phosphatidylinositol-(4,5)-bisphosphate enables efficient secretion of HIV-1 Tat by infected T-cells. *EMBO Journal* 2010; 29: 1348–1362.

[132] Jensen EC. Use of Fluorescent Probes: Their Effect on Cell Biology and Limitations. *Anatomical Record* 2012; 295: 2031–2036.

[133] Lakowicz JR. *Principles of fluorescence spectroscopy*. Springer, 2006. Epub ahead of print 2006.

[134] Ries J, Schwille P. Fluorescence correlation spectroscopy. *BioEssays* 2012; 34: 361–368.

[135] Widengren J, Mets Ü, Rigler R. Fluorescence correlation spectroscopy of triplet states in solution: A theoretical and experimental study. *Journal of Physical Chemistry* 1995; 99: 13368–13379.

[136] Benda A, Beneš M, Mareček V, et al. How to determine diffusion coefficients in planar phospholipid systems by confocal fluorescence correlation spectroscopy. *Langmuir* 2003; 19: 4120–4126.

[137] Singh V, Macharová S, Riegerová P, et al. Determining the Functional Oligomeric State of Membrane-Associated Protein Oligomers Forming Membrane Pores on Giant Lipid Vesicles. *Anal Chem* 2023; 95: 8807–8815.

[138] Šachl R, Čujová S, Singh V, et al. Functional Assay to Correlate Protein Oligomerization States with Membrane Pore Formation. *Anal Chem* 2020; 92: 14861–14866.

[139] Dimou E, Cosentino K, Platonova E, et al. Single event visualization of unconventional secretion of FGF2. *Journal of Cell Biology* 2019; 218: 683–699.

[140] Dimou E, Nickel W. Unconventional mechanisms of eukaryotic protein secretion. *Current Biology* 2018; 28: R406–R410.

[141] Stein H, Spindler S, Bonakdar N, et al. Production of isolated giant unilamellar vesicles under high salt concentrations. *Front Physiol*; 8. Epub ahead of print 13 February 2017.

[142] Angelova MI, Dimitrov DS. Liposome electroformation. *Faraday Discuss Chem Soc* 1986; 81: 303–311.

List of Figures

	resolution image can then be rebuilt using the locations of multiple localised probe molecules. The lower left inset of the second panel displays an experimental image of a single fluorescent dye (blue) alongside the high-precision localization of the molecule (red cross). (The figure was adapted from "10.1146/annurev.biochem.77.061906.092014").
Figure 7	This image represents the principle of STED microscopy. (A) The mechanism of stimulated emission. (B) A diagram illustrating a STED microscope. (C) In XY mode, a doughnut-shaped STED laser is used, with its zero point aligned to the peak of the excitation laser focus. Through saturated depletion, fluorescence from areas near the zero point is suppressed, leading to a smaller effective PSF size. (The figure was adopted from "10.1146/annurev.biochem.77.061906.092014").
Figure 8	Stepwise photobleaching methods to determine protein oligomeric states. (a) Fluorescent intensity traces for mono, di, tri, and tetrameric proteins are shown. Each stepwise drop in the fluorescence intensity versus time plot corresponds to the photobleaching of one fluorophore. (b) Single Molecule Co-Tracking: The proteins of interest are labeled with fluorophores of different spectra, and their diffusion paths in the membrane are tracked using localization algorithms. This allows direct visualization of molecular association (i), dissociation, and co-diffusion (ii and iii). (c) Fluorescent molecules are imaged based on their point spread function (PSF). Larger protein complexes do not produce a broader PSF compared to monomeric proteins, but they do exhibit a higher amplitude. Thus, analyzing the brightness of diffraction-limited spots enables the determination of the underlying oligomeric state. (The figure was adopted from "https://doi.org/10.1007/978-3-319-66601-3_8").
Figure 9	Principles of FCS measurements (A) A laser beam excites fluorescent particles as they diffuse within the detection volume. (B) The emission from these fluorophores leads to fluctuations in fluorescence intensity, which are recorded by a detector. (C) These intensity fluctuations are then correlated to

	produce an autocorrelation curve. The diffusion time τ_D is determined at the half maximum of the autocorrelation function.
Figure 10	Förster resonance energy transfer method. Nonradiative energy transfer to the (red-shifted) acceptor dye molecule happens only when the two dyes are near to each other, as in an oligomer, after the donor dye molecule is excited. The rate of the energy transfer depends strongly on the distance between the two dye molecules. (Figure was adopted from "https://doi.org/10.1007/978-3-319-66601-3_8").
Figure 11	The structure of Fibroblast Growth Factor 2 (FGF2). (The figure was adopted from "doi: 10.3389/fcell.2022.864257")
Figure 12	Unconventional protein secretion I pathway of FGF2, for bypassing the use of intracellular vesicle intermediates. Instead, it directly translocates across the plasma membrane. This figure includes all the steps in the translocation process. (The figure was adopted from "doi: 10.3389/fcell.2022.864257")
Figure 13	(A) FGF2-GFP associated with the GUV membrane, (B) Alexa-Fluor-532 probing GUV membrane permeability (C) GUV membrane labeled with DOPE-Atto-633, and panel (A+B+C) is the merged image of all three fluorescent dyes.
Figure 14	dual-color Fluorescence Correlation Spectroscopy on a single GUV involves focusing the bilayer into the beam center. The measurement begins by aligning the bilayer using the maximum red signal along the black arrow in the vertical XZ GUV plane. The correct membrane position, where the bilayer is optimally focused, is marked as "2".
Figure 15	The dual-(+1)-FCS analysis includes (A) calculating the average intensity for the monomer (<*I*(mono)>) and the oligomer (<*I*(oligo)>), as well as fitting the autocorrelation functions *G*(τ) for the monomer, oligomer, and the lipid tracer DOPE-Atto-633. (B) The fitting process provides the readout parameter mentioned in the text.

Figure 16	The GUVs shown on the left-hand side of the figure represent the GUVs in the INITIAL state. They can be either leaky or non-leaky as monitored by the in-leakage of Alexa-Fluor-532. The right-hand side of the figure represents the GUVs in the FINAL state 240 minutes after the incubation of FGF2 with the GUVs. As shown on the figure, four different cases are possible and can be distinguished from each other by adding a new aliquot of Alexa-Fluor-532.
Figure 17	The time-course of a time-resolved dual-(+1)-FCS measurement. The whole measurement takes about 315 minutes.
Figure 18	This pie chart shows that while FGF2 binds to the membrane of most GUVs during a 4-hour incubation period, some GUVs develop pores (become leaky), while others remain intact (non-leaky).
Figure 19	This figure illustrates the functional correlation between various parameters related to FGF2-GFP induced membrane pore formation. Panel (A) shows the oligomeric size of FGF2-GFP (N(m.u.)). The size of these oligomers, indicated by the number of molecules forming a complex on the membrane, is represented by each dot, which corresponds to a measurement taken from a single GUV. Panel (B) depicts the surface concentration of FGF2-GFP (PSC(FGF2-GFP)) on the GUV membrane, measured in nmol/m². A threshold concentration is marked by a dashed line with a red arrow, indicating the upper limit of the concentration range (0 to 0.3 nmol/m²) reached by 90% of nonleaky GUVs. Panel (C) presents a 2D scatter plot that simultaneously displays the correlation between oligomeric size, surface concentration. Median values and 95% confidence intervals are shown by solid black lines in panels A and B, while colored dashed lines represent median values in panel C.
Figure 20	The correlation between the oligomeric size of FGF2-GFP and lipid pore formation was monitored over time on individual GUVs. (Case A) illustrates GUVs that initially did not allow the fluorescent tracer to penetrate (GUVs without pores) but became filled with the tracer during incubation with FGF2-GFP (GUVs with pores). In contrast, Case B displays GUVs that

	remained impermeable to the small fluorescent tracer throughout the entire experiment.
Figure 21	PSC correlation with oligomeric state (an individual GUV's study in a time-resolved manner). (A) This panel shows the INITIAL State of GUVs, grey represents non-leaky and cyan is for leaky vesicles. (B) This panel shows FINAL State of vesicles e.g. black dots represents non-leaky to non-leaky GUVs.
Figure 22	Correlation of the average diffusion coefficient of FGF2 to PSC (upper row), as well as the oligomeric state to the diffusion coefficient of FGF2 (lower row) for all three populations considered throughout the work.
Figure 23	Time-dependent FGF2 oligomer sizes distribution. Top row represents leaky to leaky, middle row represents non-leaky to non-leaky and the lowest row non-leaky to leaky vesicle populations. Violin plots (A3,B3,C3) showing the distribution of PSC for each vesicle population in the Pre-INITIAL, INTITAL and FINAL states are displayed on the right-hand side of the figure.
Figure 24	Correlation of $\Delta\langle N(\text{m.u.})\rangle$ and ΔPSC against each other. Each dot represents a GUV.
Figure 25	(A) Distribution of oligomeric states of FGF2-GFP without any filtering (i.e., without classifying GUVs as leaky or non-leaky) as determined by dual-(+1)-FCS. (B) Distribution of oligomeric states for FGF2-GFP with a filter applied for leaky GUVs only. (C) The broad distribution of oligomeric states of FGF2-Y81pCMF-Halo-StarRed on supported lipid bilayers from the previous work by *Steringer et al., eLife 2017* determined by STED. (D) FGF2 oligomeric state as determined by *Dimou et al. 2018* on the plasma membranes of living cells with single molecule localisation microscopy.

List of Tables

List of Abbreviations

2D	Two Dimensional
3D	Three Dimensional
ACF	Auto correlation function
AFM	Atomic Force Microscopy
BAK	Bcl-2 homologues antagonist/killer
BAX	Bcl-2-associated protein x
BCL-2	B-cell leukemia/lymphoma 2 protein
bFGF	Basic Fibroblast Growth Factor
bis-EA	bis-(2-methanethiosulfonatoethyl) amine hydrochloride
Cryo-EM	cryo-electron microscopy
CFP	cyan fluorescent protein
D	Diffusion Coefficient
DNA	Deoxyribonucleic Acid
dual-FCS	two-color dual-colour fluorescence correlation spectroscopy
EGFP	Enhanced GFP
EM	Electron Microscopy
FCCS	Fluorescence Cross-Correlation Spectroscopy
FCS	Fluorescence Correlation Spectroscopy
FGF	Fibroblast Growth Factor Receptor
FGF1	Fibroblast Growth Factor 1
FGF2	Fibroblast Growth Factor 2
FGFR	Fibroblast Growth Factor Receptor
FPALM	fluorescent photoactivation localization microscopy
FPs	fluorescent proteins
FRET	Förster Resonance Energy Transfer
FWHM	full width at half maximum
GFP	Green Fluorescent Protein
GPC1	Glypican-1
GPI	glycosylphosphatidylinositol

GSDMs	Gasdermin
GUVs	Giant Unilamellar Vesicles
HeNe laser	Helium Neon laser
IR	Infrared
LSM	Light Sheet Microscopy
LUVs	Large Unilamellar Vesicles
m.u.	Monomeric Unit
min	Minute
mM	millimolar
MLKL	Pore Forming Proteins
MOM	Mitochondrial Membrane
mono	Monomer
N&B	Number and Brightness
NA	Numerical Aperature
nm	Nanometre
NMR	Nuclear Magnetic Resonance
oligo	Oligomer
PALM	photoactivated localization microscopy
PDL	Photo Diode Laser
PFPs	Pore Forming Proteins
PFTs	Pore Forming Toxins
PI(4,5)P2	Phosphatidylinositol 4,5-bisphosphate
PLMs	Planar Lipid Membranes
PM	Plasma Membrane
PN	Particle Number
PSC	Protein Surface Concentration
PSF	Point Spread Function
PSMs	Polymer Supported Membranes
RESOLFT	Reversible Saturable Optically Linear Fluorescence Transition
SDS-PAGE	Sodium Dodecyl Sulfate-Polyacrylamide Gel Electrophoresis
SPBs	Supported phospholipid bilayers
sm-FRET	Single-molecule Förster Resonance Energy Transfer

SMLM	Single-Molecule Localization Super-Resolution Microscopy
SP	Structure Parameter
SPBs	Supported Phospholipid Bilayers
SSIM	Saturated Structured illumination Microscopy
STED	Stimulated Emission Depletion Microscopy
STED-FCS	Stimulated Emission Depletion -FCS
STORM	stochastic optical reconstruction microscopy
SUVs	Small Unilamellar Vesicles
TCSPC	Time -Correlated Single Photon Counter
TIRF	Total Internal Fluorescence Reflection Microscopy
UPS Pathway	Unconventional Protein Secretion Pathway
YFP	yellow fluorescent protein
ΔN(m.u.)	Change in the Oligomeric State
ΔPSC	Change in the Protein Surface Concentration

List of publications

This thesis is based on two publications, both of which were published in the Analytical Chemistry journal. Further details are listed below:

Publications related to the dissertation

1) Radek Šachl, Sabína Čujová, **Vandana Singh**, Petra Riegerová, Peter Kapusta, Hans-Michael Müller, Julia P. Steringer, Martin Hof, Water Nickel. Functional Assay to Correlate Protein Oligomerization States with Membrane Pore Formation. *Anal. Chem.* **2020**, *92*, 14861-14866, https://doi.org/10.1021/acs.analchem.0c03276

Vandana's contribution to the manuscript: Vandana performed the measurements and analyzed the data together with S. Čujová and P. Riegerová. In that sense, the contribution of Vandana can be considered equal to SČ and PR contributions.

2) **Vandana Singh**, Sabína Macharová, Petra Riegerová, Julia P. Steringer, Hans-Michael Müller, Fabio Lolicato, Walter Nickel, Martin Hof, Radek Šachl. Determining the Functional Oligomeric State of Membrane-Associated Protein Oligomers Forming Membrane Pores on Giant Lipid Vesicles. Analytical Chemistry **2023**, *95* (23),8807-8815. https://doi.org/10.1021/acs.analchem.2c05692

Vandana's contribution to the manuscript: VS prepared the samples and, performed dual-(+1)-FCS measurements and analyzed the data with the help of SM and PR. She was fully involved in the preparation of the manuscript and created all the figures for the paper.

Publications with the topic unrelated to the dissertation

3) Man Thi Hong Nguyen, Denys Biriukov, Carmelo Tempra, Katarina Baxova, Hector Martinez-Seara, Hüseyin Evci, **Vandana Singh**, Radek Šachl. Martin Hof, Pavel Jungwirth, Matti Javanainen and Mario Vazdar. Ionic strength and solution

composition dictate the adsorption of cell-penetrating peptides onto phosphatidylcholine membranes. *Langmuir* **2022**, *38*, 11284-11295. https://doi.org/10.1021/acs.langmuir.2c01435

Vandana's contribution to the manuscript: VS prepared the samples for fluorescence cross-correlation spectroscopy measurements. She performed all FCCS measurements and analyzed all FCCS data together with HE.

4) Pawel Mystek; **Vandana Singh**; Matěj Horváth; Karolína Honzejková; Petra Riegerová; Huseyn Evci; Martin Hof; Tomáš Obšil; Radek Šachl. The Minimal Membrane Requirements for BAX-induced Pore Opening upon Exposure to Oxidative Stress, *accepted in Biophysical Journal*.

Vandana's contribution to the manuscript: VS prepared the samples and performed all FCCS measurements and the analysis of FCCS data. VS prepared all figures in the MS and was fully involved in writing the paper together with PM and RŠ.